

# Northumbria Research Link

Citation: Fyffe, Catriona, Woodget, Amy S., Kirkbride, Martin, Deline, Philip, Westoby, Matt and Brock, Benjamin (2020) Processes at the margins of supraglacial debris cover: quantifying dirty ice ablation and debris redistribution. *Earth Surface Processes and Landforms*, 45 (10). pp. 2272-2290. ISSN 0197-933

Published by: Wiley-Blackwell

URL: <https://doi.org/10.1002/esp.4879> <<https://doi.org/10.1002/esp.4879>>

This version was downloaded from Northumbria Research Link:  
<http://nrl.northumbria.ac.uk/id/eprint/42763/>

Northumbria University has developed Northumbria Research Link (NRL) to enable users to access the University's research output. Copyright © and moral rights for items on NRL are retained by the individual author(s) and/or other copyright owners. Single copies of full items can be reproduced, displayed or performed, and given to third parties in any format or medium for personal research or study, educational, or not-for-profit purposes without prior permission or charge, provided the authors, title and full bibliographic details are given, as well as a hyperlink and/or URL to the original metadata page. The content must not be changed in any way. Full items must not be sold commercially in any format or medium without formal permission of the copyright holder. The full policy is available online: <http://nrl.northumbria.ac.uk/policies.html>

This document may differ from the final, published version of the research and has been made available online in accordance with publisher policies. To read and/or cite from the published version of the research, please visit the publisher's website (a subscription may be required.)

# Processes at the margins of supraglacial debris cover: quantifying dirty ice ablation and debris redistribution

Catriona L Fyffe\*, Amy S. Woodget, Martin P. Kirkbride, Philip Deline, Matthew J. Westoby and Ben W. Brock

\*Northumbria University, Ellison Building, Newcastle-Upon-Tyne, NE1 8ST  
[catriona.fyffe@northumbria.ac.uk](mailto:catriona.fyffe@northumbria.ac.uk), 0191 227 3956

Keywords: Debris-covered glaciers, Østrem curve, dirty ice, Unmanned Aerial Systems, ablation

## Abstract

Current glacier ablation models have difficulty simulating the high-melt transition zone between clean and debris-covered ice. In this zone, thin debris cover is thought to increase ablation compared to clean ice, but often this cover is patchy rather than continuous. There is a need to understand ablation and debris dynamics in this transition zone to improve the accuracy of ablation models and the predictions of future debris cover extent. To quantify the ablation of partially debris-covered ice (or 'dirty ice'), a high-resolution, spatially-continuous ablation map was created from repeat unmanned aerial systems (UAS) surveys, corrected for glacier flow in a novel way using on-glacier ablation stakes. Surprisingly, ablation is similar (range ~5 mm w.e. per day) across a wide range of percentage debris covers (~30-80%) due to the opposing effects of a positive correlation between percentage debris cover and clast size, countered by a negative correlation with albedo. Once debris cover becomes continuous, ablation is significantly reduced (by 61.6% compared to a partial debris cover), and there is some evidence that the cleanest ice (<~15% debris cover) has a lower ablation than dirty ice (by 3.7%). High-resolution feature tracking of clast

29 movement revealed a strong modal clast velocity where debris was continuous,  
30 indicating that debris moves by creep down moraine slopes, in turn promoting debris  
31 cover growth at the slope toe. However, not all slope margins gain debris due to the  
32 removal of clasts by supraglacial streams. Clast velocities in the dirty ice area were  
33 twice as fast than clasts within the continuously debris-covered area, as clasts  
34 moved by sliding off their boulder tables. These new quantitative insights into the  
35 interplay between debris cover characteristics and ablation can be used to improve  
36 the treatment of dirty ice in ablation models, in turn improving estimates of glacial  
37 meltwater production.

## 38 1 Introduction

39 Ablation of partially debris-covered ice (dirty ice) is thought to be higher than ablation  
40 of both clean and completely debris-covered ice (Reid and Brock, 2010; Evatt *et al.*,  
41 2015). On debris-covered glaciers, dirty ice areas exist upglacier from the margin of  
42 the continuous debris cover, where the ablation rates are some of the highest found  
43 across the glacier (Fyffe *et al.*, 2014). The increase in the spatial extent of  
44 supraglacial debris covers, which typically operates over decadal timescales  
45 (Kirkbride and Warren, 1999; Stokes *et al.*, 2007; Bolch *et al.*, 2008; Bhambri *et al.*,  
46 2011; Thakuri *et al.*, 2014) occurs by the upglacier migration of the margin of the  
47 continuous cover, so understanding melting processes here is crucial to be able to  
48 predict future changes in debris cover and glacier mass balance. Robust predictions  
49 of glacier mass balance are imperative for accurate forecasting of future glacier  
50 runoff that considers the combined influence of climate change and changing  
51 supraglacial debris cover.

52 The Østrem curve describes the relationship between debris thickness and sub-  
53 debris ablation (Østrem, 1959; 1965). When the cover of debris is thin (defined by  
54 being less than the 'critical thickness') ablation is higher than the ablation rate for  
55 clean ice, whereas debris thicker than the critical thickness reduces ablation  
56 compared to clean ice (see Figure 2 in Kirkbride and Dugmore, 2003). This critical  
57 thickness is dependent on weather conditions and the bare ice albedo (Hagg *et al.*,  
58 2008; Lejeune *et al.*, 2013). The debris thickness resulting in the highest ablation is  
59 termed the 'effective thickness'; represented by the peak of the Østrem curve  
60 (Kirkbride and Dugmore, 2003). Thin debris increases melt by (a) decreasing albedo,

61 allowing greater absorption of incoming solar radiation, and (b) allowing the fast  
62 conduction of heat energy to the ice surface (Mattson *et al.*, 1993). Meanwhile, thick  
63 debris reduces melt because heat is lost from the surface of the debris to the  
64 atmosphere, and because the diurnal cycle is attenuated by the debris so it is  
65 reduced in amplitude at the ice-debris interface (Reznichenko *et al.*, 2010)

66 Østrem curves have been derived for several glaciers worldwide (e.g. Khan, 1989;  
67 Mattson *et al.*, 1993; Konovalov, 2000; Popovnin and Rozova, 2002; Lukas *et al.*,  
68 2005; Mihalcea *et al.*, 2006; Nicholson and Benn, 2006; Hagg *et al.*, 2008; Reid and  
69 Brock, 2010; Wang *et al.*, 2011; Brook *et al.*, 2013 (including studies on rock debris  
70 not tephra)), usually from ablation stake measurements at sites with naturally varying  
71 debris thicknesses or at artificial plots. However, thin debris covers are rarely  
72 continuous due to variations in clast thickness and redistribution by meltwater  
73 (Østrem, 1959; 1965). Ablation in areas of discontinuous debris cover is suspected  
74 to be very spatially variable, because clast thicknesses vary around the critical  
75 thickness (especially for rock debris, typically 1 to 3 cm, see Table 1), and stake  
76 measurements cannot adequately capture this variability. Enhanced melting below  
77 small clasts forms cryoconite holes (e.g. Bøggild *et al.*, 2010), whereas thicker clasts  
78 form boulder tables, from micro-tables under small clasts to examples several  
79 metres tall under large boulders.

80 Ablation modelling of partially debris-covered areas remains in its infancy. Most  
81 energy balance models presume a continuous debris cover, with ablation increasing  
82 with decreasing debris thickness, and so do not replicate the decrease in ablation for  
83 thicknesses below the effective thickness, which forms the peak in the Østrem curve  
84 (Nicholson and Benn, 2006; Zhang *et al.*, 2011; Reid *et al.*, 2012; Collier *et al.*, 2014;  
85 Rounce *et al.*, 2015). However, Reid and Brock (2010) were able to replicate the  
86 peak in the Østrem curve by varying both debris thickness and the ratio of ice to  
87 debris (or 'patchiness'). The ice-debris ratio decreased with increasing debris  
88 thickness, simulating the decrease in exposed ice as the debris thickens. Evatt *et al.*'s  
89 (2015) melt model simulates porous debris layers, and this model replicated the  
90 peak in the Østrem curve by either varying the proportion of debris cover, or by  
91 reducing the evaporative heat flux as the debris thickens. However, neither of these  
92 models have been evaluated using field data from partially debris-covered ice due to  
93 a lack of suitable data on spatially-continuous ablation, the key model input variables

94 (especially clast size and thickness, debris patchiness and albedo), and how these  
95 variables interact with each other.

96 Furthermore, a challenge for debris-covered glacier research is to determine future  
97 change in debris cover extent and thickness, which is complicated by the complex  
98 relationships between debris supply, debris thickness, sub-debris melt, surface  
99 topography and glacier dynamics. Existing studies of debris cover formation are  
100 theoretical or restricted to the glacier centre line (Anderson, 2000; Kirkbride and  
101 Deline, 2013; Anderson and Anderson, 2016; Wirbel *et al.*, 2018). Rowan *et al.*  
102 (2015) created a mass balance model that simulates debris transport (following ice  
103 flow) and the subsequent evolution of supraglacial debris cover thickness, thereby  
104 allowing the integration of the influence of debris cover on glacier mass balance.  
105 However, the local scale supraglacial debris redistribution processes were not  
106 accounted for. Moore (2018) provides a methodology for predicting instability in  
107 supraglacial debris using a theoretical approach, but current understanding of the  
108 mass movement processes relevant to supraglacial debris remains limited, mainly  
109 due to a lack of field data describing rates of debris movement and change in debris  
110 cover extent over time.

111 The generation of high-resolution orthoimagery and topographic data from UAS  
112 flights (e.g. Woodget and Austrums, 2017), combined with appropriate ground truth  
113 data (i.e. data collected on the ground), provide methods with which to improve our  
114 understanding of ablation processes in dirty ice areas. This paper analyses repeat  
115 high-resolution UAS imagery of a dirty ice region of Miage Glacier, Italy, to quantify  
116 spatially-continuous ablation and debris movement vectors at the clast scale. These  
117 data allow us to answer the following fundamental questions for the first time:

- 118 1. What is the influence of percentage debris cover, albedo, clast size and clast  
119 thickness on dirty ice ablation rates, and how do these variables interact?
- 120 2. How can clast thickness and albedo be determined from UAS outputs to  
121 facilitate modelling of dirty ice ablation?
- 122 3. What are the processes that control debris supply and remobilisation in dirty  
123 ice areas?

## 124 2 Methodology

### 125 2.1 Study site

126 Miage Glacier is completely debris-covered over its lower tongue with a mean debris  
127 thickness of 0.25 m (Foster *et al.*, 2012). The study site is a ~180 m x 200 m area of  
128 dirty ice situated between 2453 and 2484 m a.s.l., above the continuous debris  
129 cover, and between a left-lateral and medial supraglacial moraine (Figure 1). The  
130 lower portion of the site is bounded by debris deposited from an ice avalanche that  
131 originated from a gully on the northern margin of the central (Dome Glacier) tributary.  
132 The supraglacial debris at the study site is composed of a mixture of schists, gneiss  
133 and tectonic breccia (Deline, 2002), derived originally from rock fall and snow/rock  
134 avalanches from the steep valley sides (Deline, 2009). The dirty ice region between  
135 the moraines has a discontinuous cover of dust- to boulder-sized clasts, with patches  
136 of more complete cover (Figure 1). Debris is supplied to this region directly via dirt  
137 cones and the melt-out of transverse debris-filled crevasse traces, and indirectly  
138 from the surrounding moraine slopes, although occasionally rock fall and avalanches  
139 supply debris from adjacent bedrock slopes. Supraglacial streams follow the base of  
140 the left-lateral moraine (towards the north east of the study site), and the base of the  
141 medial moraine (towards the south west of the study site), and confluence to the  
142 south of stake S15 (see Figure 1).

### 143 2.2 Field data collection

#### 144 2.2.1 Survey stakes and their use as ground control points

145 Visits to Miage Glacier were conducted in July and August 2017. Prior to the first  
146 UAS survey, sixteen white plastic ablation stakes were drilled into the ice using a  
147 Heucke stream drill and were distributed across the study area so that they could be  
148 used as ground control points for subsequent georeferencing of the UAS imagery.  
149 Stakes were cut flush with the ice surface and a ground marker was added to identify  
150 stake locations in the UAS imagery (Figure 1c). Stakes were surveyed in July using  
151 a combination of a Leica VIVA GS10 differential global navigation satellite system  
152 (GNSS) and Leica Builder 500 total station (up to 0.0015 m accuracy over 100m),  
153 whereas in August solely the GNSS was used. The GNSS was composed of a base  
154 station situated on a stable boulder near Miage Lake (near the terminus of the

155 glacier) and a roving system operating on static mode. The ablation at each stake  
156 during the study period was also measured.

157 The mean quality of the July reference stake GNSS positions (as reported by Leica  
158 Geo Office software) was  $\leq 0.002$  m in XY and Z, with the ambiguities being  
159 successfully resolved in all cases. In August, the positions of two stakes were not  
160 resolved successfully. However, stakes were still sufficient in number and spatial  
161 distribution to allow georeferencing of the UAS imagery, and the quality of the  
162 successfully occupied positions was satisfactory (mean quality of  $\leq 0.005$  m in XY  
163 and Z).

164 An independent estimate of the GNSS survey error was given by occupying the S4  
165 reference stake twice, with the difference in positions equating to 0.021 m in XY and  
166 0.006 m in Z. These errors are notably larger than the software estimates likely due  
167 to the operator-induced errors involved in maintaining the GNSS staff stable over the  
168 stake location. As a result, we conservatively estimate horizontal (XY) and vertical  
169 (Z) GNSS survey errors of 0.02 m and 0.01 m respectively. Later, these errors, and  
170 others, are used to estimate the total error in the ablation maps.

#### 171 2.2.2 UAS image acquisition and processing

172 A small rotary-winged UAS, the DJI Phantom 4 Pro (P4P) quadcopter, was deployed  
173 to acquire high resolution imagery of the site on 17<sup>th</sup> July and 22<sup>nd</sup> August 2017. The  
174 P4P was flown c. 30 m above the glacier, which permitted the acquisition of imagery  
175 with a spatial resolution of c. 0.01 m. The P4P integrated camera is a 1-inch CMOS  
176 sensor, capable of recording standard optical imagery in RGB. Imagery was  
177 collected with sufficient overlap (c. 80%) to ensure successful image matching using  
178 Structure from Motion (SfM) photogrammetry. Images were acquired predominantly  
179 at nadir, with the inclusion of a smaller proportion of images (25-30% depending  
180 upon the survey date) acquired at oblique angles to mitigate against the introduction  
181 of systematic elevation errors which can result from the use of solely nadir imagery  
182 (James and Robson, 2014). Images affected by blurring or other visual artefacts  
183 were excluded, returning a total of 182 and 361 usable images for the July and  
184 August surveys.

185 Imagery was processed using SfM photogrammetry within Agisoft PhotoScan Pro  
186 version 1.4.0 (now known as Agisoft Metashape) to produce a Digital Elevation

187 Model (DEM) at 0.04 m ground sample distance (GSD) and an orthophoto at 0.009  
188 m GSD for each survey date. The mean residual errors associated with the spatial  
189 positioning of the DEM and orthophoto were computed by comparing the known  
190 positions of four reference stakes (S1-S4) which had been surveyed using the GNSS  
191 with the corresponding positions on the DEM and orthophoto. These errors equate to  
192 the spatial accuracy of these data products in XYZ and were -0.024 m and -0.010 m  
193 for the July and August surveys, respectively. The mean residual errors in Z only (i.e.  
194 mean elevation errors) were -0.065 m and -0.038 m for the July and August surveys,  
195 respectively.

### 196 2.2.3 Data collected on the ground

197 Fifty 0.5 x 0.5 m quadrats were established during the July field campaign only  
198 (Figure 1a-b). Close-range quadrat photographs (hereafter 'ground truth  
199 photographs') were taken on the 19<sup>th</sup> and 22<sup>nd</sup> of July 2017, after the acquisition of  
200 UAS imagery. The four corners of the quadrats were georeferenced using the total  
201 station and GNSS. The quadrat corner locations were then used to georeference the  
202 close-range ground truth photographs into ArcGIS v10.5.1 using a projective  
203 transformation.

204 The albedo of 25 of these quadrats was measured using a Kipp and Zonen CM7B  
205 albedometer (sensitive in the wavelength range 0.3-2.8  $\mu\text{m}$ , with a pyranometer  
206 accuracy of +/- 2%) held level at a height of 1 m from the surface, around 0.5 m  
207 from the fieldworker, while ensuring the sensors were not shaded. Albedo  
208 measurements were made between 13:08 and 15:15 on the 22<sup>nd</sup> of July under  
209 mainly cloudy conditions. While ice albedo is observed to increase under cloudy  
210 conditions, due to a shift in the incoming solar radiation to shorter wavelengths, the  
211 effect is small for light to moderately cloudy conditions and for ice affected by light  
212 absorbing impurities (Brock, 2004). Based on observations of albedo under cloudy  
213 conditions by Brock (2004), which were made on bright, clean ice where cloud  
214 effects are enhanced, we estimate the uncertainty of the albedo measurements to be  
215 +/- 5%.

216 At seven quadrats the dimensions of all but the smallest clasts (A-axis less than ~  
217 0.01 m) were measured by hand. The A- and B-axis (as seen from above) and the

218 clast thickness (not necessarily the C-axis) were measured. Once measurements  
219 were complete, the clasts were redistributed over the ice surface within the quadrat.

220 Sample points within each quadrat were selected by placing a regular 0.05 x 0.05 m  
221 grid across each quadrat in ArcGIS (Figure 1b). At each point the surface was  
222 classified as ice or debris by eye, based on the ground truth photographs. The A-  
223 and B-axis dimensions of each clast which fell beneath a sample point were also  
224 measured using the scaled and georeferenced photograph. The clast axes were  
225 digitised by hand. Some clasts were not measured, either because they fell partially  
226 outside of the quadrat, were too small to identify or were obscured by other clasts.  
227 On average 29 clasts were measured per quadrat. The A- and B-axes  
228 measurements identified from the ground truth photographs give information only on  
229 the surface clasts. Grain size statistics (mean,  $D_{50}$  and  $D_{84}$ ) were calculated for each  
230 quadrat.

## 231 2.3 Data analysis

### 232 2.3.1 Spatially continuous ablation

233 To calculate continuous ablation over the one-month interval between UAS surveys,  
234 corrections to the August DEM were required to take account of the horizontal and  
235 vertical components of glacier flow. To achieve the horizontal shift, the August DEM  
236 was spatially repositioned to align with the July DEM, using a first-order polynomial  
237 (affine) transformation based on the horizontal (XY) change in location of the stakes  
238 between the two surveys. The spatial variation in horizontal velocity and the  
239 residuals from the affine transformation are shown at the stake locations in Figure  
240 S1ab in the Supplementary Information.

241 To compute the total horizontal error ( $\epsilon$ ) within the resulting ablation map, three error  
242 sources were combined:

- 243 1. The mean XY error associated with transforming the August DEM to align with  
244 the July DEM ( $\alpha = 0.129$  m).
- 245 2. The residual XY errors for each epoch - i.e. the difference between the positions  
246 of markers S1, S4, S8 and S12 from the GNSS data and their corresponding  
247 positions on the orthoimagery generated from the UAS-SfM approach (given in  
248 Table S1 in the Supplementary Information). Equation 1 was used to compute  
249 combined XY residual errors for each survey epoch ( $\phi$ ) rather than individual X

250 and Y values, with Equation 2 used to propagate the residual error across both  
 251 survey epochs ( $\beta = 0.048$  m).

$$252 \quad \varphi_{Epoch} = \sqrt{(X^2 + Y^2)} \quad \text{Eq. 1}$$

$$253 \quad \beta = \sqrt{(\varphi_{July})^2 + (\varphi_{August})^2} \quad \text{Eq. 2}$$

254 3. The GNSS survey error, as reported in section 2.2.1 ( $\theta = 0.02$  m).

255 The sum of these three errors ( $\alpha$ ,  $\beta$  and  $\theta$ ) equates to 0.197 m, which gives a  
 256 conservative estimate of the total XY error associated with the ablation map.

257 To determine ablation, it was necessary to account for the elevation change caused  
 258 by down-valley glacier flow and the ice emergence velocity (which describes the  
 259 vertical component of glacier flow in the ablation zone). This was computed as the  
 260 difference between measured stake ablation and the vertical height change  
 261 measured at each stake using the GNSS-total station data. Using ablation stakes as  
 262 control points allowed the combined slope and emergence value to be quantified  
 263 explicitly, instead of estimating these terms (c.f. Rounce *et al.* (2018)). The variation  
 264 in the combined slope and emergence value did not show a clear spatial pattern  
 265 across the survey area (Figure S1c in Supplementary Information) and ranged from  
 266 0.59 to 0.67 m. As a result, the mean value (0.62 m) was applied as a uniform  
 267 positive vertical shift to the August DEM.

268 We calculated ablation between the two surveys by subtracting the re-positioned and  
 269 vertically corrected August DEM from the July DEM using 2.5D differencing. Mean  
 270 ablation was calculated at a range of scales, specifically  $\times 50$ ,  $\times 100$  and  $\times 150$   
 271 multipliers of the orthophoto ground sample distance (GSD), equating to cell sizes of  
 272  $\sim 0.47$  m, 0.95 m and 1.42 m, respectively). We restrict our analysis of ablation data  
 273 to  $\times 50$  GSD and above (or of mean values within the 0.5 x 0.5 m quadrats) because  
 274 this multiplier exceeds the horizontal error of the ablation data (0.197 m).

275 To assess the overall accuracy of the spatially-continuous ablation map, measured  
 276 stake ablation was compared with the mapped ablation values, giving a root mean  
 277 square error (RMSE) of 1.45 mm w.e. per day, equating to 0.059 m over the 36 day  
 278 study period, or 2.7% compared to the mean stake surface loss. Ablation values  
 279 may be influenced by boulder movement, producing artificial 'ice loss' (July) and 'ice  
 280 gain' (August) pairings. To remove this effect for large boulders, ablation within the

281 dirty ice region (see Figure 1a) <40 or >70 mm w.e. per day were excluded from  
282 further analysis, equating to 3.3% and 2.6% of the ablation data within the dirty ice  
283 region, respectively. These threshold values were determined after iteration to allow  
284 the removal of ablation data which were obviously attributable to boulder movement,  
285 while maintaining the majority of the ablation data. The removed ablation data  
286 (Figure S2, Supplementary Information) is restricted to boulder shaped pairs, except  
287 for some areas of very high melt following the main streams, small areas of low melt  
288 where the debris is continuous near the boundary of the region, and at the stream  
289 confluence where boulders accumulated in the channel. The movement of small  
290 clasts is unlikely to have a significant influence on the mapped ablation values since  
291 the mean measured clast thickness (0.014 m) was lower than the error in the  
292 ablation map, and clast movement into a cell will be balanced by clast movement out  
293 of a cell, so that the overall influence on ice loss should be minimal. Negative  
294 ablation values outside of the dirty ice area were also removed. Ablation within the  
295 quadrats was checked for clast movement: this resulted in quadrats QAP and QD  
296 being excluded from analysis. Other quadrats were excluded due to georeferencing  
297 issues (QAS) or because they fell outside of the spatially continuous ablation map  
298 (QAX and QO).

### 299 2.3.2 Percentage debris cover

300 Percentage debris cover was determined for each survey using two methods: 'point'  
301 and 'orthophoto'. The 'point' method involved determining the percentage debris  
302 cover from the ice/debris classification of the surface beneath each of the sample  
303 points within each quadrat (see section 2.2.3 and Figure 1b). The 'orthophoto'  
304 method involved classification of the July and August orthophotos into debris or ice  
305 using a maximum probability method. Training sites for the classification were  
306 located within the quadrats, using a similar number of 'ice' and 'debris' cells. The  
307 July and August orthophotos were classified separately to account for differences in  
308 illumination. The training sites used for classification were similar in number and  
309 distribution across both survey epochs. The resulting debris/ice classifications (cell  
310 size ~0.01 x 0.01 m) were then used to determine the percentage debris cover at a  
311 range of scales (section 2.3.1).

312 The point method of deriving the percentage debris cover is more reliable since the  
313 surface cover beneath each point is known, although the surface cover is only

314 sampled. The orthophoto method was evaluated by classifying the orthophoto by eye  
315 for each image at 249 equally spaced points, giving a producers accuracy (derived  
316 from the number of correctly classified points divided by the number of points known  
317 to be in that class) for the July (August) classification of 89% (95%) for debris and  
318 49% (49%) for ice. Ice cover is therefore underrepresented by the classification  
319 approach due to relatively dark ice being misclassified as debris. This explains why  
320 the orthophoto method overestimates the percentage cover compared with the point  
321 method (Figure 2). The exception to this is when the point method estimates 100%  
322 debris cover, and lower values are given within the orthophoto method, a  
323 consequence of misclassification of light-coloured debris as ice. However, the  
324 orthophoto method allows the determination of the percentage debris cover across  
325 the entire study area.

### 326 2.3.3 Debris cover change

327 The change in the debris cover between the two surveys was quantified using three  
328 approaches. First, the difference in orthophoto percentage debris cover between July  
329 and August was calculated at three scales (50, 100 and 150 x Orthophoto GSD).  
330 Second, the change in cover type was quantified by manually delimiting the  
331 boundary between the dirty and continuously debris-covered area (e.g. Figure 1a).  
332 Finally, individual clast movement was manually tracked. Clasts were chosen by  
333 creating sample points extracted from a 7.46 m regular grid created over the study  
334 area. At each sample point, the nearest clast which could be clearly identified as the  
335 same clast in both the July and August orthoimages was tracked by creating a line  
336 joining the same point on the clast in both images, which produced 295 individual  
337 clast tracks. These tracks were used to determine the clast velocity, directional  
338 bearing, boulder a-axis length (from the July orthophoto), and the surface slope, to  
339 explore their influence on clast movement. The surface slope was extracted at the  
340 July boulder position from the August DEM (resampled to 1 m cell size), to reduce  
341 the likelihood of the slope value being influenced by surface expression of the clast  
342 in the DEM data. To examine small scale clast movement dynamics at the debris/ice  
343 boundary clast tracking was repeated at a smaller scale over a region of debris-  
344 cover gain.

## 345 3 Results

### 346 3.1 Spatially-continuous ablation

347 The high resolution (0.04 m GSD) map of spatially-continuous ablation is presented  
348 in Figure 3. The efficacy of the 'ablation stakes as control points' methodology is  
349 clearly demonstrated by the excellent visual correspondence of ablation with the  
350 surface cover shown in the orthophotos (Figure 3). Surface melt rates vary between  
351 c.30 mm w.e. per day on areas of thick and continuous debris on the moraine crests,  
352 to c.60 mm w.e. per day in areas of partial debris cover. Thinner but continuous  
353 debris on moraine edges and cleaner ice within the inter-moraine area have slightly  
354 lower ablation rates of c.50 mm w.e. per day.

355 The highest melt rates of up to 65 mm w.e. per day occur along the supraglacial  
356 streams. Stream locations remained stable due to incision, shown by the narrow  
357 bands of high melt following the channels. Drainage lines in areas of complete debris  
358 cover are also observed as lines of increased ablation, which manifest as  
359 downslope-oriented stripes on the south-western moraine, a radial pattern in the  
360 central part of the north-eastern moraine, and an almost anabranching network on  
361 the moraine towards the east of the study site (Figure 3). These drainage lines  
362 represent the locations of sub-debris supraglacial streams, which can be observed  
363 emerging at the base of the moraines and in areas of thinner debris following the  
364 ablation patterns. Previous dye tracing and debris excavation revealed sub-debris  
365 streams/preferential flow paths under complete debris lower on the glacier (Fyffe *et*  
366 *al.*, 2019). Increased ablation may be a result of heat transfer from the supraglacial  
367 stream water, or the local reduction in debris thickness due to the removal of debris  
368 by hydraulic action.

### 369 3.2 The influence of surface characteristics on dirty ice ablation

#### 370 3.2.1 Percentage debris cover and ablation

371 A surprising finding is the remarkably constant ablation across a wide range of  
372 percentage debris covers (Figure 4). A near-complete debris cover comprised of a  
373 layer of single clasts has an ablation rate similar to much lower percentage covers -  
374 e.g. QE with a 97% single-clast cover has almost the same ablation as QL which has  
375 a 19% cover, Figure 4. At moderate percentage debris covers (c. 30-80%), ablation  
376 is enhanced compared to both the cleanest and more debris-covered ice but there is

377 not a clear peak in melt rate where the enhancement is maximised. Melt rate values  
378 in the quadrat data range between 55 and 60 mm w.e. per day (mean 57.3 mm w.e.  
379 per day,  $\sigma$  1.5 mm w.e. per day) (Figure 4). A similar pattern is also found in the  
380 continuous data (Figure 5), with ablation high but very similar where the debris cover  
381 is less than approximately 60%, and the variability in ablation within each 10% debris  
382 cover band being noticeably lower for moderate percentage covers.

383 The quadrat data also show a very abrupt decrease in ablation when the debris  
384 cover is close to complete and is, importantly, multiple clasts thick (Figure 4). This  
385 can be quantified by comparing the mean ablation of the quadrats with a 30-80%  
386 cover (57.3 mm w.e. per day) with the mean ablation of the quadrats with a 100%  
387 cover (35.5 mm w.e. per day), giving a melt reduction compared to the partially  
388 covered quadrats of 61.6%. Ablation decreases as soon as the debris layer is  
389 multiple clasts thick, with quadrats with smaller clasts (and therefore likely thinner  
390 debris thicknesses) exhibiting higher ablation rates compared to those with larger  
391 clasts (see QAZ and QAT in Figure 4). This decrease in ablation when the cover  
392 becomes close to complete is not as abrupt in the continuous data, likely due to  
393 misclassification of lighter coloured debris as ice (Figure 5).

394 When the percentage debris cover is very low (<15%) there is evidence that ice  
395 melts at slightly lower rates than in areas with a higher percentage debris cover (15  
396 to ~80%). This is shown in Figure 4, where quadrats with point percentage debris  
397 covers up to 15% (QAA, QAF, QAM, QAN and QT (QS excluded as a stream  
398 influenced ablation)) have a mean ablation of 55.3 mm w.e. per day (range 55.0-55.9  
399 mm w.e. per day). In contrast, quadrats with 15-20% cover (QAL, QAY, QJ, QL)  
400 have a mean ablation of 57.8 mm w.e. per day (range 57.4-58.3 mm w.e. per day)  
401 and quadrats with a 30-80% debris cover have a mean ablation of 57.3 mm w.e. per  
402 day (range 54.6-59.3 mm w.e. per day). If the 0-15% cover is taken as 'clean ice' and  
403 the 30-80% cover taken as 'dirty ice', the melt enhancement due to an incomplete  
404 debris cover is 3.7% compared to clean ice. The difference in ablation is small but  
405 measurable, given the RMSE of the continuous ablation map is 1.45 mm w.e. per  
406 day. As the percentage cover increases, the quadrat data shows a gradual increase  
407 in melt rate, corresponding to an increase in clast size (from a mean A-axis  $D_{50}$  of 8  
408 mm for the 0-15% group, to 12 mm for the 15-20% group, and 23 mm for the 30-80%  
409 group). At low percentage covers, clasts tend to be thin enough to melt into the ice

410 surface, with the intervening ice maintaining a white colour (and presumably high  
411 albedo) due to the formation of a weathering crust (Figure 4). The continuous data  
412 also show lower mean ablation at the smallest percentage debris covers (rounded to  
413 0%) compared to mean ablation at moderate percentage debris covers (10-30% or  
414 greater) at 50 x and 100 x GSD (Figure 5). However this pattern is not seen at 150 x  
415 GSD (although there were only 8 cells in the 0% group using the July orthophoto and  
416 none in August) (Figure 5).

417 The overall relationship between ablation and percentage debris cover (using the  
418 quadrat data shown in Figure 6b) is quadratic ( $R^2$  (Adj) = 0.524,  $p < 0.01$ , excluding  
419 QS). A negative linear relationship is also significant, but is not as strong ( $R^2$  (Adj) =  
420 0.305,  $p < 0.01$ , excluding QS). This better fit of the quadratic relationship compared  
421 to the linear relationship lends confidence to the interpretation of lower ablation  
422 occurring at the smallest percentage debris covers, since the linear fit cannot  
423 describe the decrease in ablation at small percentage covers and is instead  
424 dominated by the low ablation of the quadrats with the highest percentage debris  
425 cover. A quadratic relationship also better describes the relationship between mean  
426 ablation and percentage debris cover for each 10% debris cover group using the  
427 continuous data (Figure 5). However, we note that the relative rarity of very clean ice  
428 in the continuous data and the fairly small decrease in ablation measured in both the  
429 quadrat and continuous datasets means that there is some uncertainty whether the  
430 cleanest ice really has a lower ablation than that with a moderate percentage cover.

### 431 3.2.2 The influence of clast size, clast thickness and albedo on ablation

432 Ablation correlates significantly with clast size, albedo and elevation for all quadrats  
433 (Column A, Table 2), but these relationships collapse when only partially debris-  
434 covered quadrats are included (Figure 6, Figure 7a and Column B in Table 2).  
435 Therefore, none of these debris characteristics determines dirty ice ablation rates on  
436 its own. When completely debris-covered quadrats (which have larger clasts, lower  
437 albedo and higher elevations) are included, their lower ablation influences results  
438 (see Table 2). Albedo was found to negatively correlate with ablation of partially  
439 covered quadrats, but only if the quadrats included had a percentage cover less than  
440 50% ( $r = -0.635$   $p < 0.05$   $R^2$  (adj) = 0.329). Measurements of clast thickness at seven  
441 quadrats revealed no significant relationship with ablation (Figure 8a), likely because  
442 of the differences in percentage cover and albedo.

### 443 3.3 Determining clast thickness and albedo from imagery

#### 444 3.3.1 Albedo and its relationship with clast size and percentage debris cover

445 Albedo and percentage debris cover have a strong negative relationship (Column C  
446 in Table 2 and Figure 7b). However, it is noteworthy that a second order polynomial  
447 provides a stronger relationship between albedo and point percentage cover than a  
448 straight line ( $R^2$  (Adj) = 0.751 and 0.661 for a quadratic and linear relationship,  
449 respectively), demonstrating that the change in albedo is greatest at small  
450 percentage covers (~0-40%). As the percentage cover increases further, albedo  
451 declines more slowly. Albedo has a negative relationship with clast size (Table 2,  
452 Figure 7c). However, there is an important interrelationship between percentage  
453 debris cover and clast size (Figure 7d), with the strongest correlation being between  
454 point percentage cover and mean B-axis ( $r_s = 0.798$   $p < 0.01$ ). The partial correlation  
455 between albedo and point percentage cover controlling for mean B-axis remains  
456 strong and significant ( $r = -0.567$   $p < 0.01$ ), whereas the partial correlation between  
457 albedo and mean B-axis controlling for percentage cover becomes insignificant. The  
458 percentage cover is therefore the key determinant of albedo, rather than the clast  
459 size.

#### 460 3.3.2 Determining clast thickness

461 Clast thickness is an important variable when simulating dirty ice melt (Evatt *et al.*,  
462 2015) which cannot be determined directly from either ground or aerial imagery.  
463 However, the field measurements of mean and  $D_{50}$  values of clast thickness within  
464 the quadrats (0.5 m x 0.5 m) showed strong correlations with both measured and  
465 ground truth image clast size, with strong correlations also between clast thickness  
466 and percentage cover (Figure 8 and Table 3). Clast thickness could therefore be  
467 inferred from either clast size or percentage debris cover at a 0.5 m x 0.5 m scale.

### 468 3.4 Debris supply and remobilisation

469 No overall increase in the percentage debris cover between July and August was  
470 detected. However, close inspection of Figures 9 and 10 reveals a pattern of ice  
471 surface evolution. Fine debris and melt-retarding clasts were washed into hollows  
472 and stream channels, increasing debris cover there. The location of the debris-  
473 trapping hollows in August matches with areas of higher percentage debris cover in  
474 the July imagery. Meanwhile, the intervening ice hummocks experienced a decrease

475 in percentage cover, with clasts thin enough to melt into the ice forming cryoconite  
476 holes. Overall, the concentration of debris in the hollows increases while the  
477 intervening ice becomes cleaner, with the transverse crevasse traces becoming less  
478 distinct as a result (Figure 10). Primary supply of debris from melt-out of crevasse  
479 traces therefore has not resulted in a uniform increase in debris cover.

480 Clast feature tracking demonstrates that clasts move by different mechanisms in the  
481 debris-covered and dirty ice areas (shown in Figures 11a and 12). Clast velocity in  
482 the debris-covered area had a strong histogram mode (0.015 m per day, based on a  
483 0.01 m per day bin size), with a similar median (0.016 m per day) and small standard  
484 deviation (0.026 m per day). Clast velocity is only very weakly influenced by slope  
485 ( $R^2$  (Adj) = 0.070), and moderately influenced by clast A-axis length ( $R^2$  (Adj) =  
486 0.371). These findings are consistent with a gradual downslope creep of the debris  
487 matrix, where clasts slide downslope due to gravity over the melting ice surface, but  
488 with their velocities impeded by their downslope neighbours. Small-scale clast  
489 feature tracking (Figure 11c) demonstrates the increase in clast velocity as clasts are  
490 released from the debris matrix and into the dirty ice area.

491 In the dirty ice area, the average clast velocity (0.042 m per day) was twice that in  
492 the debris-covered area (0.022 m per day) and had a larger standard deviation  
493 (0.047 m per day). However, the histogram mode (0.015 m per day) was the same  
494 as for the debris-covered area. The relationship between clast velocity and clast A-  
495 axis length is stronger than in the debris-covered area ( $R^2$ (Adj) = 0.526) and the  
496 slope has a greater (if still very weak) influence ( $R^2$  (Adj) = 0.132). The greater clast  
497 velocities are not an artefact of sampling larger clasts in the dirty ice area, since  
498 Figure 12a shows that the clast velocity remains higher in the dirty ice area  
499 compared to the debris-covered area for a given clast A-axis length. This suggests  
500 clasts move via a topple-walk mechanism, whereby clasts retard ablation beneath  
501 them and build an ice pedestal, before sliding off this pedestal and coming to rest  
502 downslope. Larger ice pedestals will be formed by larger (and likely thicker)  
503 boulders, resulting in longer travel distances, explaining the relation of clast velocity  
504 with clast size. The more erratic slide direction evident in Figure 11a, compared to on  
505 the debris-covered slopes, is further evidence of this movement mechanism.

506 Debris creep from moraine slopes supplies material to the dirty ice area. However,  
507 there are areas of debris loss as well as debris gain along the moraine margins.  
508 Overall 284 m<sup>2</sup> of debris-covered area became dirty ice, whereas 342 m<sup>2</sup> of dirty ice  
509 area became debris-covered, resulting in a net gain of 58 m<sup>2</sup> of debris cover (Figure  
510 11b). The mean debris gain distance (calculated from the minimum bounding  
511 rectangle for each area of gain or loss) was 1.26 m, equating to a rate of change of  
512 0.035 m per day, similar to the debris clast velocities measured through feature  
513 tracking. The mean debris loss distance was 1.01 m, equating to 0.028 m per day.  
514 The loss of debris is caused by stream erosion removing debris during floods, since  
515 areas of gain and loss were found along the south-western medial moraine, whose  
516 margin is close to the main western stream, whereas debris was consistently gained  
517 along the margin of the south-eastern moraine which is far from any streams. Note  
518 that by August the branch of the eastern stream closest to the north-eastern moraine  
519 had been diverted further west.

520 Faster melting of dirty ice resulted in a greater lowering of this surface compared to  
521 the debris-covered moraine slopes (Figure 13), with a consequent increase in the  
522 gradient of the moraine slopes over time (by 1.5° on average). This increase in  
523 gradient decreased with distance downglacier, except for section 1 of the eastern  
524 slope. An increase in slope gradient could be caused by an increase in ablation with  
525 distance downslope, which is evident in Figure 13d. This suggests that the debris  
526 thins with distance down the moraine slopes.

## 527 4 Discussion

### 528 4.1 Understanding ablation in dirty ice areas

529 The high-resolution ablation map gives a new insight into the melting of partially  
530 debris-covered ice (Figure 3). There is some evidence that only the cleanest ice  
531 (less than ~15% debris cover) has lower ablation than partially debris-covered ice.  
532 This may explain why some studies (Hagg *et al.*, 2008; Brook *et al.*, 2013) did not  
533 detect enhanced ablation beneath a thin debris cover: their 'clean-ice' may not have  
534 been sufficiently free of debris. A slight covering of cryoconite (similar to QAL in  
535 Figure 4) or a layer of dust on the surface (Adhikary *et al.*, 2000), would be enough  
536 to enhance ablation compared to completely clean ice. The initial increase in ablation  
537 with percentage debris cover up to ~20% is due to an increasing cover of small

538 clasts which decrease albedo. At low percentage debris covers, albedo decreases  
539 most sharply with increasing cover (Figure 7b) and there is an inverse relationship  
540 between albedo and ablation (Figure 7a). Under moderate covers (~30-80%)  
541 ablation is remarkably constant, and it is inferred that this is due to the contrasting  
542 role of albedo and clast size. As the percentage debris cover increases, albedo is  
543 reduced (Figure 7b), which is known to increase ablation by increasing the net  
544 shortwave radiation received by a surface (Brock *et al.*, 2000). However,  
545 simultaneously the clast size tends to increase (Figure 7d), corresponding with  
546 thicker clasts which are likely to reduce ablation, given the known reduction in  
547 ablation with increasing debris thickness (e.g. Østrem, 1959; 1965).

548 The quadrat data showed that melting reduces significantly as soon as the debris  
549 cover becomes close to complete and multiple clasts thick (Figure 4). Østrem curve  
550 theory suggests that very thin debris covers enhance ablation compared to clean ice  
551 (Østrem, 1959). However, a thin continuous cover which increased ablation  
552 compared to clean ice was rarely observed. Instead, partial debris cover enhanced  
553 melting compared to clean ice, but melting reduced as soon as the debris cover was  
554 near complete (which seemed to correspond with a layer multiple clasts thick). This  
555 suggests that the 'patchiness' approach devised by Reid and Brock (2010) holds  
556 promise, since many of the characteristics of their modelling were also displayed in  
557 the data collected (debris thickness increased with percentage debris cover following  
558 an exponential delay function, and albedo also decreased with percentage cover).

#### 559 4.2 Providing a basis for modelling melt in dirty ice areas

560 The field data provide a basis for simulating dirty ice ablation. Percentage debris  
561 cover has been determined successfully from orthophotos using a maximum  
562 probability classification, although the spectral signatures of ice and debris do  
563 overlap. More complex methods such as object-based image analysis (e.g.  
564 Kraaijenbrink *et al.*, 2016) could be employed instead. A strong relationship between  
565 albedo and percentage debris cover allows albedo to be derived from mapped  
566 percentage debris cover, although it could also be directly determined from  
567 orthophoto brightness (following Corripio (2004)). Clast thickness correlates strongly  
568 with both percentage debris cover and clast A-axis, meaning it could be estimated  
569 from percentage debris cover or clast size distribution maps. Clast size has been  
570 derived for river environments from both point cloud roughness and image texture

571 (Carbonneau *et al.*, 2005; Woodget and Austrums, 2017; Woodget *et al.*, 2017). If  
572 this methodology were applied to dirty ice environments, it would allow clast size  
573 (and therefore clast thickness) to vary independently from percentage cover. This  
574 might be useful for modelling as it would allow situations such as smaller clasts  
575 forming a near complete cover to be modelled correctly.

576 Mapping spatially-continuous ablation using 'ablation stakes as control points' could  
577 revolutionise the validation of spatially-distributed melt models. Testing models  
578 against a map of ablation will give a clear picture of where they are performing  
579 successfully or not. The map (Figure 3) highlights the importance of supraglacial  
580 streams on ablation, including hidden sub-debris streams. Melt models do not  
581 routinely include melting along supraglacial stream courses, but this phenomenon  
582 could be significant to overall melt volumes.

#### 583 4.3 Ice surface and debris cover evolution

584 The detailed analysis of clast movement and surface change presented contributes  
585 to a coherent understanding of the glaciological and slope processes leading to  
586 debris cover formation and evolution, as shown in Figure 14. Primary debris supply  
587 to the dirty ice area is from the melt out of crevasse fills and dispersed englacial  
588 debris. Debris released from crevasse traces is rapidly remobilised by melt and  
589 rainwater and concentrated into hollows and streams (Figure 10). Downslope clast  
590 movement from moraine flanks provides debris to the margins of the dirty ice area  
591 (section 3.4). Overall there was a net gain of debris along the moraine/dirty ice  
592 margins, but locally, removal of debris also occurs.

593 In models of debris cover evolution (Anderson, 2000; Rowan *et al.*, 2015; Anderson  
594 and Anderson, 2016) ablation rate and englacial debris concentration determine the  
595 rate of supraglacial debris accumulation. Mechanisms of debris removal from the  
596 surface are not accounted for: such models conserve debris until it either reaches  
597 the margins or the glacier tongue becomes stationary. Observations at Miage Glacier  
598 show that rainfall and meltwater removes fine debris from the dirty ice surface and  
599 washes clasts from ice hummocks into hollows. Overbank flows in supraglacial  
600 streams will remove clasts from their adjacent ice surfaces (Figure 14). Debris  
601 entrained by surface streams will be transported through the supraglacial-englacial-  
602 subglacial stream network to eventually leave the glacier, although some may return

603 to glacial transport (e.g. Kirkbride and Spedding, 1996). Future modelling of debris  
604 cover evolution should therefore account for loss as well as gain of supraglacial  
605 debris, especially in transitional areas of high melt and partial debris cover. This  
606 could be incorporated in a simple manner (e.g. by applying that a fraction of debris  
607 gained on an ice surface is lost to the hydrological network), but more work is  
608 needed to quantify the importance of hydrological transport within the debris-glacier  
609 system.

610 The transition from a partial to a complete debris cover not only reduces ablation  
611 (see section 3.2 above), but also reduces the removal of the fine fraction of the  
612 debris. Fine debris trapped within a complete cover is less likely to be removed,  
613 since any rain or meltwater will be forced to travel slowly through the debris matrix.  
614 The fines fraction affects the debris thermal conductivity and moisture content, which  
615 are likely to differ markedly from a single clast layer. At the study site, a continuous  
616 debris cover is caused mainly by the encroachment of debris from moraine slopes,  
617 rather than by melt out of englacial debris. This contrasts with nearby Glacier  
618 d'Estelette, where transverse debris bands have a high rate of debris emergence,  
619 sufficient to cause complete debris cover formation (Kirkbride and Deline, 2013).  
620 This difference is explained by the location of the Miage Glacier study site, which  
621 although below the ELA, is relatively high in the ablation area. Kirkbride and Deline  
622 (2013) found that debris outcrop emergence was enhanced down-glacier for reasons  
623 including slower ice flow, and shallower and more closely spaced debris septa.

624 Analysis of the clast velocities suggest that clasts travel down moraine slopes by  
625 creep (slow continuous sliding) processes, whereas clasts within the dirty ice area  
626 move by the topple-walk mechanism (section 3.4, Figure 14). Anderson (2000)  
627 modelled topple-walk movements down moraine slopes. Although this was observed  
628 on the margins and within the dirty ice area, this mechanism was not observed on  
629 the debris-covered moraine slopes where there is no differential ablation or boulder  
630 table formation. Future modelling work should therefore adjust the movement  
631 mechanism depending upon the surface type. The modal clast velocity values and  
632 velocity distributions from Miage Glacier provide a basis for simulating clast  
633 velocities in future work.

634 Although Moore (2017) focusses on modelling the location of debris instability rather  
635 than all mass movement mechanisms (including creep, which does not require  
636 instability), the prediction of movement down the face of moraine slopes and  
637 hydraulic erosion in the valleys between moraine ridges do qualitatively agree with  
638 our data. Moore's (2017) analysis assumes a constant debris thickness, inconsistent  
639 with the decrease in debris thickness found with distance down the moraine slopes  
640 (Figure 13d). However, Moore's (2017)  $Z$  value (the ratio of debris transmissivity to  
641 meltwater supply rate) becomes smaller (equating to greater instability) as the debris  
642 thickness decreases, which may explain the increase in clast velocities near the  
643 moraine toe (Figure 11). Equally however these faster velocities could be explained  
644 by local destabilisation at the foot of the slope (due to fluvial erosion or debris  
645 thinning reducing the buttressing effect of the debris matrix on the upslope debris),  
646 which invalidates the assumption of negligible longitudinal forces in the infinite slope  
647 analysis (Moore, 2018).

648 The increase in ablation downslope in Figure 13d implies that the debris thickness  
649 decreases downslope, causing a gradient in ablation. The downslope thinning of the  
650 debris cover may be the result of debris transfer to the dirty ice area at the foot of the  
651 slope and/or higher debris supply rates near the moraine crest. The gradient in  
652 ablation down the moraine slope causes the moraine to steepen over time (Figure  
653 13). This process of moraine steepening exemplifies the 'waxing' stage of medial  
654 moraine development of Small and Clark (1974), a morphological response to  
655 differential ablation between the debris-covered moraine and adjacent clean ice. In  
656 contrast, these results do not agree with Anderson (2000), in which the medial  
657 moraine slope angle and down-slope debris thickness were prescribed constant  
658 values. Anderson's (2000) modelled moraine slopes therefore grew inward,  
659 increasing the debris cover at the expense of clean ice. Future models of moraine  
660 evolution should therefore include a down slope decrease in debris thickness.

#### 661 4.4 Future recommendations

662 The above analysis result in a series of recommendations for future modelling of  
663 ablation and debris cover evolution. Spatially-continuous ablation maps constructed  
664 by the 'ablation stakes as control points' methodology would provide an excellent  
665 validation dataset for distributed ablation models. Distributed modelling of dirty ice  
666 ablation is clearly possible, since percentage debris cover can be determined from

667 the classification of UAS orthophotos, with albedo relating strongly to the percentage  
668 debris cover. Mean clast thickness can be determined from mean clast size, which  
669 can be found from percentage debris cover, although clast size could be determined  
670 separately via other methods (e.g. point cloud roughness or image texture  
671 (Carbonneau *et al.*, 2005; Woodget and Austrums, 2017; Woodget *et al.*, 2017)) if it  
672 was required to vary separately from percentage debris cover in the modelling  
673 regime. The consistent increase in ablation across debris covers from 30-80% could  
674 allow a simpler modelling approach whereby these areas are identified and ablation  
675 enhanced uniformly relative to clean ice. Results from plot scale studies, where  
676 clean ice is artificially loaded with debris of different thicknesses to infer its influence  
677 on melt rate, should be interpreted with caution. In reality, thin debris covers are  
678 rarely continuous and the interactions between albedo, percentage debris cover and  
679 clast size/thickness, which have an important impact on melt rate, may be neglected.

680 The clast velocity statistics for the dirty ice (median 0.025 m per day) and debris-  
681 covered areas (median 0.016 m per day), or the exponentially modified Gaussian  
682 distributions found, could be used in future models of debris cover evolution. It is  
683 also clear that different debris movement mechanisms should be applied for different  
684 surface covers. Moraine slopes are also likely to have a downslope decrease in  
685 debris thickness. The loss of debris from the dirty ice surface due to stream erosion  
686 results in not all debris transported to the ice surface contributing to debris cover  
687 creation. Future work is necessary to quantify the percentage loss of debris to the  
688 glacier hydrological system.

## 689 5 Conclusion

690 Detailed analysis of repeat UAS-SfM orthoimagery and DEMs acquired over an area  
691 of dirty ice has provided a unique insight into the influence of a partial debris cover  
692 on ablation and the processes of debris movement and cover formation. It was found  
693 that very high resolution (0.04 m GSD), accurate (RMSE 1.45 mm w.e. per day) and  
694 spatially continuous maps of ablation can be produced by combining repeat UAS  
695 imagery with field measurements of the horizontal and vertical components of glacial  
696 flow (the 'ablation stakes as control points' methodology). The resulting ablation  
697 map was of a high enough quality to distinguish patterns of ablation attributed to  
698 variations in percentage debris cover and the influence of sub-debris streams.

699 A traditional Østrem curve approach where ablation is related to debris thickness is  
700 not appropriate for regions with a partial debris cover under high melt conditions  
701 because of the complex interrelationships between clast thickness, clast size,  
702 percentage debris cover and albedo. These interrelationships result in ablation  
703 remaining remarkably consistent (quadrat ablation ranged from 54.6 to 59.3 mm w.e.  
704 per day) across a range of percentage debris covers (30-80%). This consistency is  
705 likely due to the competing effects of albedo and clast thickness: albedo decreases  
706 with an increase in percentage debris cover (increasing ablation), meanwhile clast  
707 size (which correlates with clast thickness) increases with percentage cover  
708 (decreasing ablation). However, there is evidence that partially debris-covered ice  
709 had higher ablation (by 3.7%) than the cleanest ice (<15% debris cover). This initial  
710 increase in ablation with increasing percentage debris cover is due to a decrease in  
711 albedo. Conversely, when the debris is multiple clasts thick and forms an almost  
712 continuous cover, ablation decreases by 61.6% compared to a partial cover. The  
713 completion of the debris cover is therefore a key threshold because the subsequent  
714 trapping of finer debris will result in further changes to the thermal conductivity and  
715 moisture properties of the layer.

716 Analysis of clast movement and change in the debris cover between surveys  
717 revealed that debris is transferred down moraine slopes to dirty ice areas via creep  
718 processes, producing areas of debris gain at the moraine-dirty ice margin. Areas of  
719 debris loss also occurred due to stream water erosion. In the dirty ice area debris  
720 travels across the ice surface via a topple-walk mechanism. Debris emerging from  
721 fine transverse crevasse traces was re-distributed by melt and rainwater into hollows  
722 and streams in the dirty ice area. Ablation increased down the moraine slopes,  
723 implying a downslope decrease in debris thickness, which is the likely cause of the  
724 progressive steepening of the moraine slopes over time.

## 725 6 Acknowledgements

726 We would like to thank the British Society for Geomorphology for funding this work  
727 and the NERC Geophysical Equipment Facility (loan 1087) for providing the loan of  
728 two GNSS receivers. The authors are also grateful to Gwilym Luckett (employed  
729 through the University of Worcester VRAS scheme), John Barrow (supported by the  
730 University of Worcester), Amelia Andrews and Fiona White for their invaluable help

731 in the field. We also thank the team of the Fondazione Montagna Sicura for their  
732 assistance during the August field trip. We are grateful to an anonymous reviewer  
733 and Ann Rowan for their helpful and constructive comments on the manuscript.

## 734 7 Data Availability

735 The data sets produced and analysed during the current study are available at  
736 10.5281/zenodo.3749317. Reasonable requests to access the data will be granted  
737 by the corresponding author.

## 738 8 Conflict of interest

739 The authors declare no conflict of interest.

## 740 9 References

- 741 Adhikary, S., Nakawo, M., Seko, K. and Shakya, B. (2000) Dust influence on melting process  
742 of glacier ice: experimental results from Lirung Glacier, Nepal Himalayas, *Debris Covered*  
743 *Glaciers: IAHS*, 264, pp. 43–52. doi: 10.1111/insp.12083.
- 744 Anderson, L. S. (2014) *Glacier Response to Climate Change: Modeling the Effects of Weather*  
745 *and Debris-Cover*.
- 746 Anderson, L. S. and Anderson, R. S. (2016) Modeling debris-covered glaciers: response to  
747 steady debris deposition, *Cryosphere*, 10, pp. 1105–1124. doi: 10.5194/tc-10-1105-2016.
- 748 Anderson, R. S. (2000) A model of ablation-dominated medial moraines and the generation  
749 of debris-mantled glacier snouts, *Journal of Glaciology*, 46(154), pp. 459–469. doi:  
750 10.3189/172756500781833025.
- 751 Bhambri, R., Bolch, T., Chaujar, R. K. and Kulshreshtha, S. C. (2011) Glacier changes in the  
752 Garhwal Himalaya, India, from 1968 to 2006 based on remote sensing, *Journal of Glaciology*,  
753 57(203), pp. 543–556. doi: 10.3189/002214311796905604.
- 754 Bøggild, C. E., Brandt, R. E., Brown, K. J. and Warren, S. G. (2010) The ablation zone in  
755 northeast greenland: Ice types, albedos and impurities, *Journal of Glaciology*, 56(195), pp.  
756 101–113. doi: 10.3189/002214310791190776.
- 757 Bolch, T., Buchroithner, M., Pieczonka, T. and Kunert, A. (2008) Planimetric and volumetric  
758 glacier changes in the Khumbu Himal, Nepal, since 1962 using Corona, Landsat TM and  
759 ASTER data, *Journal of Glaciology*, 54(187), pp. 592–600. doi:  
760 10.3189/002214308786570782.
- 761 Brock, B. W. (2004) An analysis of short-term albedo variations at Haut Glacier d’Arolla,  
762 Switzerland, *Geografiska Annaler: Series A, Physical Geography*, 86 A(1), pp. 53–65. doi:  
763 10.1111/j.0435-3676.2004.00213.x.
- 764 Brock, B. W., Willis, I. C. and Sharp, M. J. (2000) Measurement and parameterization of

- 765 albedo variations at Haut Glacier d'Arolla, Switzerland, *Journal of Glaciology*, 46(155), pp.  
766 675–688.
- 767 Brook, M. S., Hagg, W. and Winkler, S. (2013) Debris cover and surface melt at a temperate  
768 maritime alpine glacier: Franz Josef Glacier, New Zealand, *New Zealand Journal of Geology  
769 and Geophysics*, 56(1), pp. 27–38. doi: 10.1080/00288306.2012.736391.
- 770 Carbonneau, P. E., Bergeron, N. E., Lane, S. N. and Wiley, J. (2005) Texture-based image  
771 segmentation applied to the quantification of superficial sand in salmonid river gravels, 127,  
772 pp. 121–127. doi: 10.1002/esp.1140.
- 773 Collier, E., Nicholson, L. I., Brock, B. W., Maussion, F., Essery, R. and Bush, A. B. G. (2014)  
774 Representing moisture fluxes and phase changes in glacier debris cover using a reservoir  
775 approach, *Cryosphere*, 8(4), pp. 1429–1444. doi: 10.5194/tc-8-1429-2014.
- 776 Corripio, J. G. (2004) Snow surface albedo estimation using terrestrial photography,  
777 *International Journal of Remote Sensing*, 25(24), pp. 5705–5729. doi:  
778 10.1080/01431160410001709002.
- 779 Deline, P. (2002) *Etude géomorphologique des interactions écroulements rocheux/glaciers  
780 dans la haute montagne alpine (versant sud-est du Massif du Mont Blanc)*. Université de  
781 Savoie, Chambéry.
- 782 Deline, P. (2009) Interactions between rock avalanches and glaciers in the Mont Blanc  
783 massif during the late Holocene, *Quaternary Science Reviews*, 28(11–12), pp. 1070–1083.  
784 doi: 10.1016/j.quascirev.2008.09.025.
- 785 Evatt, G. W., Abrahams, I. D., Heil, M., Mayer, C., Kingslake, J., Mitchell, S. L., Fowler, A. C.  
786 and Clark, C. D. (2015) Glacial melt under a porous debris layer, *Journal of Glaciology*,  
787 61(229), pp. 825–836. doi: 10.3189/2015JoG14J235.
- 788 Foster, L. A., Brock, B. W., Cutler, M. E. J. and Diotri, F. (2012) A physically based method for  
789 estimating supraglacial debris thickness from thermal band remote-sensing data, *Journal of  
790 Glaciology*, 58(210), pp. 677–691. doi: 10.3189/2012JoG11J194.
- 791 Fyffe, C., Brock, B., Miles, E. and Pellicciotti, F. (2019) Water flow through supraglacial  
792 debris, in *IGS British Branch Meeting (poster)*.
- 793 Fyffe, C. L., Reid, T. D., Brock, B. W., Kirkbride, M. P., Diolaiuti, G., Smiraglia, C. and Diotri, F.  
794 (2014) A distributed energy-balance melt model of an alpine debris-covered glacier, *Journal  
795 of Glaciology*, 60(221), pp. 587–602. doi: 10.3189/2014JoG13J148.
- 796 Hagg, W., Mayer, C., Lambrecht, A. and Helm, A. (2008) Sub-debris melt rates on southern  
797 Inylchek Glacier, central Tian Shan, *Geografiska Annaler, Series A: Physical Geography*, 90  
798 A(1), pp. 55–63. doi: 10.1111/j.1468-0459.2008.00333.x.
- 799 James, M. R. and Robson, S. (2014) Mitigating systematic error in topographic models  
800 derived from UAV and ground-based image networks, *Earth Surface Processes and  
801 Landforms*, 39(10), pp. 1413–1420. doi: 10.1002/esp.3609.
- 802 Kayastha, R. B., Takeuchi, Y., Nakawo, M. and Ageta, Y. (2000) Practical prediction of ice  
803 melting beneath various thickness of debris cover on Khumbu Glacier, Nepal, using a  
804 positive degree-day factor, *Debris-Covered Glaciers; IAHS Publication*, (264), pp. 71–81.

- 805 Khan, M. I. (1989) *Ablation on Barpu Glacier, Karakoram Himalaya, Pakistan: A study of melt*  
806 *processes on a faceted, debris-covered ice surface.*
- 807 Kirkbride, M. P. and Deline, P. (2013) The formation of supraglacial debris covers by primary  
808 dispersal from transverse englacial debris bands, *Earth Surface Processes and Landforms*,  
809 38(15), pp. 1779–1792. doi: 10.1002/esp.3416.
- 810 Kirkbride, M. P. and Dugmore, A. J. (2003) Glaciological response to distal tephra fallout  
811 from the 1947 eruption of Hekla, south Iceland, *Journal of Glaciology*, 49(166), pp. 420–428.
- 812 Kirkbride, M. P. and Spedding, N. (1996) The influence of englacial drainage on sediment-  
813 transport pathways and till texture of temperate valley glaciers, *Annals of Glaciology*, 22, pp.  
814 160–166.
- 815 Kirkbride, M. P. and Warren, C. R. (1999) Tasman Glacier, New Zealand: 20th-century  
816 thinning and predicted calving retreat, *Global and Planetary Change*, 22(1–4), pp. 11–28.  
817 doi: 10.1016/S0921-8181(99)00021-1.
- 818 Konovalov, V. (2000) Computations of melting under moraine as a part of regional modelling  
819 of glacier runoff, *Debris-Covered Glaciers; IAHS Publication*, 264, pp. 109–118.
- 820 Kraaijenbrink, P. D. A., Shea, J. M., Pellicciotti, F., de Jong, S. M. and Immerzeel, W. W.  
821 (2016) Object-based analysis of unmanned aerial vehicle imagery to map and characterise  
822 surface features on a debris-covered glacier, *Remote Sensing of Environment*, 186, pp. 581–  
823 595. doi: 10.1016/j.rse.2016.09.013.
- 824 Lejeune, Y., Bertrand, J., Wagnon, P. and Morin, S. (2013) A physically based model of the  
825 year-round surface energy and mass balance of debris-covered glaciers, *Journal of*  
826 *Glaciology*, 59(214), pp. 327–344. doi: 10.3189/2013JoG12J149.
- 827 Loomis, S. R. (1970) Morphology and ablation processes on glacier ice, in *Bushnell, V. C. and*  
828 *Ragle, R. H. (eds.) Icefield Ranges Research Project, Scientific Results, Vol 2.* New York:  
829 American Geographical Society, pp. 27–31.
- 830 Lukas, S., Nicholson, L. I., Ross, F. H. and Humlum, O. (2005) Formation, meltout processes  
831 and landscape alteration of high-arctic ice-cored moraines - Examples from Nordenskiöld  
832 land, central Spitsbergen, *Polar Geography*, 29(3), pp. 157–187. doi: 10.1080/789610198.
- 833 Mattson, L. E., Gardner, J. S. and Young, G. J. (1993) Ablation on Debris Covered Glaciers: an  
834 Example from the Rakhiot Glacier, Punjab, Himalaya, in *Snow and Glacier Hydrology, IAHS*  
835 *Publication*, pp. 289–296.
- 836 Mihalcea, C., Mayer, C., Diolaiuti, G., D'Agata, C., Smiraglia, C., Lambrecht, A., Vuillermoz, E.  
837 and Tartari, G. (2008) Spatial distribution of debris thickness and melting from remote-  
838 sensing and meteorological data, at debris-covered Baltoro glacier, Karakoram, Pakistan,  
839 *Annals of Glaciology*, 48(July 2004), pp. 49–57. doi: 10.3189/172756408784700680.
- 840 Mihalcea, C., Mayer, C., Diolaiuti, G., Lambrecht, A., Smiraglia, C. and Tartari, G. (2006) Ice  
841 ablation and meteorological conditions on the debris-covered area of Baltoro glacier,  
842 Karakoram, Pakistan, *Annals of Glaciology*, 43(1894), pp. 292–300.
- 843 Moore, P. L. (2018) Stability of supraglacial debris, *Earth Surface Processes and Landforms*,  
844 43, pp. 285–297. doi: 10.1002/esp.4244.

- 845 Nicholson, L. and Benn, D. I. (2006) Calculating ice melt beneath a debris layer using  
846 meteorological data, *Journal of Glaciology*, 52(178), pp. 463–470. doi:  
847 10.3189/172756506781828584.
- 848 Østrem, G. (1959) Ice melting under a thin layer of moraine, and the existence of ice cores in  
849 moraine ridges, *Geografiska Annaler*, 41(4), pp. 228–230.
- 850 Østrem, G. (1965) Problems of Dating Ice-Cored Moraines, *Geografiska Annaler. Series A,*  
851 *Physical Geography*, 47(1), pp. 1–38.
- 852 Popovnin, V. V and Rozova, A. V (2002) Influence of Sub-Debris Thawing on Ablation and  
853 Runoff of the Djankuat Glacier in the Caucasus, *Nordic Hydrology*, 33(1), pp. 75–94.
- 854 Reid, T. D. and Brock, B. W. (2010) An energy-balance model for debris-covered glaciers  
855 including heat conduction through the debris layer, *Journal of Glaciology*, 56(199), pp. 903–  
856 916. doi: 10.3189/002214310794457218.
- 857 Reid, T. D., Carenzo, M., Pellicciotti, F. and Brock, B. W. (2012) Including debris cover effects  
858 in a distributed model of glacier ablation, *Journal of Geophysical Research Atmospheres*,  
859 117(17), pp. 1–42. doi: 10.1029/2012JD017795.
- 860 Reznichenko, N., Davies, T., Shulmeister, J. and McSaveney, M. (2010) Effects of debris on  
861 ice-surface melting rates: an experimental study, *Journal of Glaciology*, 56(197), pp. 384–  
862 394. doi: 10.3189/002214310792447725.
- 863 Rounce, D. R., King, O., McCarthy, M., Shean, D. E. and Salerno, F. (2018) Quantifying Debris  
864 Thickness of Debris-Covered Glaciers in the Everest Region of Nepal Through Inversion of a  
865 Subdebris Melt Model, *Journal of Geophysical Research: Earth Surface*, 123, pp. 1094–1115.  
866 doi: 10.1029/2017JF004395.
- 867 Rounce, D. R., Quincey, D. J. and McKinney, D. C. (2015) Debris-covered energy balance  
868 model for Imja-Lhotse Shar Glacier in the Everest region of Nepal, *Cryosphere*, 9(3), pp.  
869 3503–3540. doi: 10.5194/tcd-9-3503-2015.
- 870 Rowan, A. V., Egholm, D. L., Quincey, D. J. and Glasser, N. F. (2015) Modelling the feedbacks  
871 between mass balance, ice flow and debris transport to predict the response to climate  
872 change of debris-covered glaciers in the Himalaya, *Earth and Planetary Science Letters*.  
873 Elsevier B.V., 430, pp. 427–438. doi: 10.1016/j.epsl.2015.09.004.
- 874 Small, R. J. and Clark, M. J. (1974) The medial moraines of the lower glacier de Tsidjiore  
875 Nouve, Valais, Switzerland, *Journal of Glaciology*, 13(68), pp. 255–263.
- 876 Stokes, C. R., Popovnin, V., Aleynikov, A., Gurney, S. D. and Shahgedanova, M. (2007) Recent  
877 glacier retreat in the Caucasus Mountains, Russia, and associated increase in supraglacial  
878 debris cover and supra-/proglacial lake development, *Annals of Glaciology*, 46, pp. 195–203.
- 879 Syverson, K. M. and Mickelson, D. M. (1993) Ablation of debris-covered ice and the  
880 formation of pitted outwash plains at Burroughs Glacier, Southeastern Alaska, in  
881 *Proceedings of the third Glacier Bay Science Symposium*, pp. 66–74.
- 882 Takeuchi, Y., Kayastha, R. B. and Nakawo, M. (2000) Characteristics of ablation and heat  
883 balance in debris-free and debris-covered areas on Khumbu Glacier, Nepal Himalayas, in the  
884 pre-monsoon season, *Debris-Covered Glaciers; IAHS Publication*, 264, pp. 53–61.

- 885 Thakuri, S., Salerno, F., Smiraglia, C., Bolch, T., D'Agata, C., Viviano, G. and Tartari, G. (2014)  
886 Tracing glacier changes since the 1960s on the south slope of Mt. Everest (central Southern  
887 Himalaya) using optical satellite imagery, *Cryosphere*, 8(4), pp. 1297–1315. doi: 10.5194/tc-  
888 8-1297-2014.
- 889 Wang, L., Li, Z. and Wang, F. (2011) Spatial distribution of the Debris Layer on glaciers of the  
890 Tuomuer Peak, Western Tian Shan, *Journal of Earth Science*, 22(4), pp. 528–538. doi:  
891 10.1007/s12583-011-0205-6.
- 892 Wirbel, A., Jarosch, A. H. and Nicholson, L. (2018) Modelling debris transport within glaciers  
893 by advection in a full-Stokes ice flow model, *The Cryosphere*, 12, pp. 189–204.
- 894 Woodget, A. S. and Austrums, R. (2017) Subaerial gravel size measurement using  
895 topographic data derived from a UAV-SfM approach, *Earth Surface Processes and*  
896 *Landforms*. doi: 10.1002/esp.4139.
- 897 Woodget, A. S., Fyffe, C. and Carbonneau, P. E. (2017) From manned to unmanned aircraft:  
898 Adapting airborne particle size mapping methodologies to the characteristics of sUAS and  
899 SfM, *Earth Surface Processes and Landforms*. doi: 10.1002/esp.4285.
- 900 Zandbelt, B. (2014) exGauss Matlab code. Available at:  
901 <http://dx.doi.org/10.6084/m9.figshare.971318>.
- 902 Zhang, Y., Fujita, K., Liu, S., Liu, Q. and Nuimura, T. (2011) Distribution of debris thickness  
903 and its effect on ice melt at Hailuoguo glacier, southeastern Tibetan Plateau, using in situ  
904 surveys and ASTER imagery, *Journal of Glaciology*, 57(206), pp. 1147–1157. doi:  
905 10.3189/002214311798843331.
- 906
- 907

908  
909  
910

Table 1 Studies of the influence of debris on ablation, concentrating on the findings relating to enhanced ablation compared to clean ice. Studies based on measurements of the influence of tephra on ablation have been excluded for brevity.

Reference	Glacier	Findings on increased ablation
<b>(Østrem, 1959, 1965)</b>	Isfallsglaciären, Tarfala, Swedish Lapland	Melt water erosion meant that measurements of enhanced ablation beneath thin layers were difficult to obtain. Critical thickness around 0.5 cm of sand.
<b>Loomis (1970)</b>	Kaskawulsh Glacier, Yukon	Ablation beneath thin debris resulted in an ablation rate 129% of bare ice ablation.
<b>Small and Clark (1974)</b>	Tsidjiore Nouve, Valais, Switzerland	Ablation beneath patches of debris 2-3 cm 117.3% of bare ice, bare ice between dispersed debris patches, 125.7% of bare ice. 1 cm fine debris also increases ablation (172.3% and 121.9% of bare ice for sites 2 and 4, respectively).
<b>Khan (1989)</b>	Barpu Glacier, Karakoram Himalaya	Critical thickness 3 cm and effective thickness 1 cm, with ablation almost doubled under 1 cm debris thickness compared to bare ice.
<b>Mattson et al., (1993)</b>	Rakhiot Glacier, Punjab, Himalaya	Critical thickness 3 cm and effective thickness 1 cm. Debris movement was greater where debris was thinner and ablation higher.
<b>Syverson and Mickelson (1993)</b>	Burroughs Glacier, Alaska	Enhanced ablation seen initially (after 2-4 days) for plots with 0.5 cm sand, 0.5 cm till and 1 cm till but by the end of the study period ablation was retarded or the same as clean ice (0.5 cm sand). This lack of enhanced ablation thought due to the maritime climate. Heavy rainfall removed most of the debris from the plots.
<b>Adhikary et al. (2000)</b>	Lirung Glacier, Nepal Himalaya	Critical dust thickness 1.33 mm (0.6 kg m <sup>-2</sup> ), effective dust thickness 0.25 mm (0.112 kg m <sup>-2</sup> ). Dust particles were washed off the surface due to meltwater. The dust reduced albedo values, although they then increased over time. The influence of dust on ablation was greater on a cliff compared to flat surface.
<b>Kayastha et al. (2000); Takeuchi et al. (2000)</b>	Khumbu Glacier, Nepal Himalayas	Critical thickness 5 cm, effective thickness 0.3 cm.
<b>Konovalov (2000)</b>	Glaciers of central Asia, Caucasus and Altai	Critical thickness 1 cm and effective thickness 0.2 cm.
<b>Popovnin and Rozova (2002)</b>	Djankuat Glacier, Caucasus	Critical thickness 7-8 cm, effective thickness 2 cm, with ablation under 2 cm 135% of clean ice. Critical thickness thought high due to packing of debris.
<b>Hagg et al. (2008)</b>	Southern Inylchek Glacier, Tian Shan.	Clean ice ablation was not exceeded at any of the plots with debris, however the bare ice plots were not completely clean.
<b>Mihalcea et al. (2008)</b>	Baltoro Glacier, Karakoram	Mention that where debris was very thin the variable debris cover altered ablation rates.
<b>Brook et al., (2013)</b>	Franz Josef Glacier, New Zealand	Clean ice ablation was not exceeded at any of the plots with debris, thought due to bare ice plots not being completely clean.
<b>Anderson (2014)</b>	Kennicott Glacier, Alaska	Enhanced ablation detected with effective thickness 1 cm, although ablation rates variable when debris < 3 cm thick.

911

912

913 *Table 2 Statistics of ablation for each quadrat against surface characteristics. Since there are several measures*  
 914 *of percentage cover and clast size only the measure with the highest correlation or regression value is given.*  
 915 *Linear regression values are only given where correlation is significant. \*The point percent measure of*  
 916 *percentage debris cover was the only measure which correlated significantly with ablation, note also that in these*  
 917 *statistics QS was included. \*\*Higher correlations/regressions were found with the August orthophoto but since the*  
 918 *albedo was measured in July the relationships with the July orthophoto are given.*

	(A) Ablation of all quadrats	(B) Ablation of partially covered quadrats	(C) Albedo
<b>Percentage debris cover</b>	Point Percent* $r_s = -0.498$ $p < 0.01$ $R^2$ (adj) = 0.312 $p < 0.01$	July Ortho Percent $r_s = 0.134$ $p = 0.134$	Point Percent $r_s = -0.811$ $p < 0.01$ $R^2$ (adj) = 0.751 $p < 0.01$ (quadratic) July Ortho Percent** $r_s = -0.631$ $p < 0.01$ $R^2$ (adj) = 0.611 $p < 0.01$ (linear)
<b>Image clast size</b>	B-axis $D_{50}$ $r_s = -0.390$ $p < 0.01$ $R^2$ (adj) = 0.367 $p < 0.01$	A-axis $D_{50}$ $r_s = 0.104$ $p = 0.564$	B-axis Mean $r_s = -0.774$ $p < 0.01$ $R^2$ (adj) = 0.500 $p < 0.01$
<b>Number of measured clasts</b>	$r_s = -0.110$ $p = 0.484$	$r_s = 0.095$ $p = 0.600$	$r_s = -0.701$ $p < 0.01$ $R^2$ (adj) = 0.571 $p < 0.01$
<b>Albedo</b>	$r_s = 0.461$ $p < 0.05$ $R^2$ (adj) = 0.089 $p = 0.096$	$r_s = 0.258$ $p = 0.286$	
<b>Elevation</b>	$r_s = -0.440$ $p < 0.01$ $R^2$ (adj) = 0.236 $p < 0.01$	$r_s = -0.249$ $p = 0.149$	
<b>Aspect</b>	$r_s = -0.078$ $p = 0.609$	$r_s = -0.033$ $p = 0.849$	

919

920 *Table 3 Statistics between clast characteristics of the quadrats where clasts were measured in the field. Since*  
 921 *there are several measures of clast size, clast thickness and percentage cover only the measures with the*  
 922 *highest correlation and regression are given. The slightly lower  $R^2$  value for the relationship of clast thickness*  
 923 *with percentage debris cover compared to measured clast size is due to the outlier at a 60% point percentage*  
 924 *cover in Figure 8b – this quadrat has a high percentage debris cover with relatively small, thin clasts.*

	Image clast size (ground truth)	Measured clast size	Percentage debris cover
<b>Clast thickness</b>	A-axis $D_{50}$ and Thickness $D_{50}$ $r = 0.868$ $p < 0.05$ $R^2$ (adj) = 0.691 $p < 0.05$	A-axis Mean and Thickness Mean $r = 0.966$ $p < 0.000$ $R^2$ (adj) = 0.921 $p < 0.01$	Point Percent and Thickness $D_{50}$ $r_s = 0.955$ $p = 0.001$ $R^2$ (adj) = 0.721 $p = 0.01$ Aug Ortho Percent and Thickness $D_{50}$ $r = 0.869$ $p < 0.05$ $R^2$ (adj) = 0.707 $p = 0.05$
<b>Image clast size (ground truth)</b>	-	A-axis $D_{50}$ $r = 0.925$ $p < 0.000$ $R^2$ (adj) = 0.819 $p < 0.01$ B-axis Mean $r = 0.927$ $p < 0.01$ $R^2$ (adj) = 0.823 $p < 0.01$	-

925

926

927

928 *Figure 1 a) Study site map of the dirty ice area showing the location of the ground control points (which were also*  
 929 *ablation stakes) and quadrats, with the inset showing the location of the study site on Miage Glacier and the*  
 930 *location of the upper and lower weather stations (UWS and LWS, respectively). Quadrats named 'Q\*' were*  
 931 *photographed on 19/07/2017 and quadrats named 'QA\*' were photographed on 22/07/2019, with their albedo*  
 932 *also measured. b) Example of the classification of the sample points on the ground truth photographs. The*  
 933 *example shown is of quadrat QA. All the yellow points would be classified as debris to determine the percentage*  
 934 *debris cover using the point method. c) Photograph of a control point flag over a stake. The red cap is resting on*  
 935 *the top of the stake and the total station survey pole is located in the centre of the cap.*

936

937 *Figure 2 Comparison of percentage debris cover derived for each of the quadrats using the 'point' and*  
 938 *'orthophoto' methods (see text for details).*

939

940

941 *Figure 3 Spatially-continuous ablation over the study area between the 17<sup>th</sup> of July and 22<sup>nd</sup> of August. Insets b*  
 942 *and d show subsets indicated by rectangles on the ablation map, with insets c and e showing the July orthophoto*  
 943 *for the same area. Note that within the dirty ice region ablation <40 mm w.e. per day or > 70 mm w.e. per day has*  
 944 *been removed to reduce the influence of boulder movement on the ablation data used for analysis. This has also*  
 945 *affected some cells of very high ablation following the main supraglacial streams. Negative values outside the*  
 946 *dirty ice area were also removed.*

947

948 *Figure 4 Ablation against debris cover using the mean ablation within each quadrat and the point percentage*  
 949 *debris cover, alongside the debris characteristics. The lower panels are an extract from the top panel to show*  
 950 *more detail for 0-20% and 80-100%. Note that the ablation of QS was influenced by a stream on one side of the*  
 951 *quadrat (explaining the large range of ablation within the quadrat shown in Figure 6b) and the ablation of QAH*  
 952 *may be influenced by an ice cliff which appeared during the survey period. QAA has cover of cryoconite between*  
 953 *the quadrats in the black and red circles in the left panel. QAN has a moderate cover of gravel sized cryoconite*  
 954 *surrounded by particularly clean ice. Although QR has a 100% debris cover as derived by the point method,*  
 955 *some ice is exposed.*

956

957

958 *Figure 5 Relationship between orthophoto percentage debris cover and ablation. Subplots a) and b) show*  
 959 *boxplots of ablation, split by the orthophoto debris cover rounded to the nearest 10%, (for July and August,*  
 960 *respectively) at a 100 x GSD scale. In subplots c) and d) the mean ablation for each 10% group of orthophoto*  
 961 *debris cover (for July and August, respectively) is shown at a range of scales (50 x, 100 x and 150 x GSD).*  
 962 *Quadratic relationships are shown as they have higher R<sup>2</sup> values than their straight-line equivalents, with*  
 963 *p<0.001 in all cases. The data cover the entire study area, except within the dirty ice region where ablation less*  
 964 *than 40 mm w.e. per day or greater than 70 mm w.e. per day was removed to reduce the influence of boulder*  
 965 *movement on analysis.*

966

967 *Figure 6 Quadrat ablation against a) percentage debris cover derived using different methods, b) point*  
 968 *percentage debris cover, c) clast size, d) number of clasts measured, e) elevation and f) aspect. Closed circles*  
 969 *are for quadrats with a partial percentage debris cover (<100% using the point percentage cover) and open*  
 970 *circles are those with a complete cover. The variation in percentage cover of low ablation points in panel a) will*  
 971 *be due to the misclassification of light-coloured debris as ice. In panel b) error bars show the maximum and*  
 972 *minimum ablation within the quadrat and the linear (blue) and quadratic (red) relationships, both significant with*  
 973 *p<0.05. These relationships do not include QS (0% debris cover) since its ablation was partly altered by a*  
 974 *stream, resulting in the wide ablation range for this point.*

975

976 *Figure 7 Quadrat albedo against a) quadrat ablation, b) percentage debris cover and c) clast size. Plot d) shows*  
 977 *the relationship between point percentage debris cover and clast size ( $r_s = 0.798$   $p < 0.01$ ,  $R^2$  (adj) = 0.624*  
 978  *$p < 0.01$ ). Where linear or quadratic regressions are shown the relationships are significant with  $p < 0.01$  in all*  
 979 *cases.*

980

981 *Figure 8 Measured clast data, with a) ablation against clast thickness, b) clast thickness against percentage*  
 982 *debris cover, c) clast thickness against clast A-axis and d) image against measured clast size. Note that the*  
 983 *relationships shown are for those measures that gave the highest correlation and regression for each variable,*  
 984 *and all are significant with  $p < 0.05$ . The larger measured compared to ground truth image clast size demonstrated*  
 985 *in panel d) will likely be due to the difficulty of measuring the smallest clasts by hand in the field. There are only 6*  
 986 *points in the datasets of image clast size because for one quadrat no clasts were found beneath the sample*  
 987 *points in the imagery.*

988

989 *Figure 9 Small scale debris cover change. Each column 1 to 3 covers the same area, as marked in panel 4. The*  
 990 *top row shows the change in percentage debris cover at 50 x GSD (where a positive debris cover difference*  
 991 *marks an increase in percentage debris cover), the second row shows the orthophoto in July and the bottom row*  
 992 *shows the orthophoto in August. The August orthophoto used to determine percentage debris cover was*  
 993 *corrected for the horizontal movement of the ice.*

994

995 *Figure 10 Ice surface evolution, a) showing the redistribution of debris from crevasse traces and b) the*  
 996 *concentration of clasts into hollows and streams alongside the removal of fine debris from ice. July and August*  
 997 *frames show the same area of the ice surface.*

998

999 *Figure 11 a) Clast track velocity determined by manual clast tracking. The arrows are orientated by the bearing of*  
 1000 *the clast track and coloured by the clast velocity. b) Change in continuous debris cover over time. Note that the*  
 1001 *margin between dirty and debris-covered ice was less distinguishable at the top of the north-eastern moraine*  
 1002 *where a large loss of debris is mapped. c) Feature tracking of clasts at a small scale on the boundary between*  
 1003 *the debris and dirty ice area. This region experienced a gain in debris cover at the debris margin between July*  
 1004 *and August. The red rectangle on the inset map shows the location of the study region.*

1005

1006 *Figure 12 Clast feature tracking, with a) relationship between clast velocity and clast A-axis length (note*  
 1007 *logarithmic x and y-axis), b) relationship between clast velocity and slope (note logarithmic y-axis), c) histogram*  
 1008 *of clast velocities with exponentially modified Gaussian distributions overlaid (fitted using Matlab code by*  
 1009 *Zandbelt (2014)), although the clast velocities can also be modelled with an exponential function (in green) for*  
 1010 *the partial debris cover, and d) histogram of bearings of clast movement vectors. All relationships shown are*  
 1011 *significant with  $p < 0.001$ .*

1012

1013 *Figure 13 Elevation cross-sections, with a) showing the cross-section locations, b) the slope gradients (with  $D_{top}$*   
 1014 *and  $D_{bot}$  the location on the cross profile of the top and bottom of the slope measured, respectively, and  $m_j$  and*  
 1015  *$m_a$  the gradient of the slope in July and August, respectively), c) the cross-section profiles with the boundary*  
 1016 *between the dirty ice and debris-covered areas marked with points, and d) ablation values extracted following the*  
 1017 *same cross-profiles.*

1018

1019

1020

1021 *Figure 14 Processes of debris supply, transport and removal occurring within the dirty ice area.*

1022

For Peer Review

## Supplementary Information

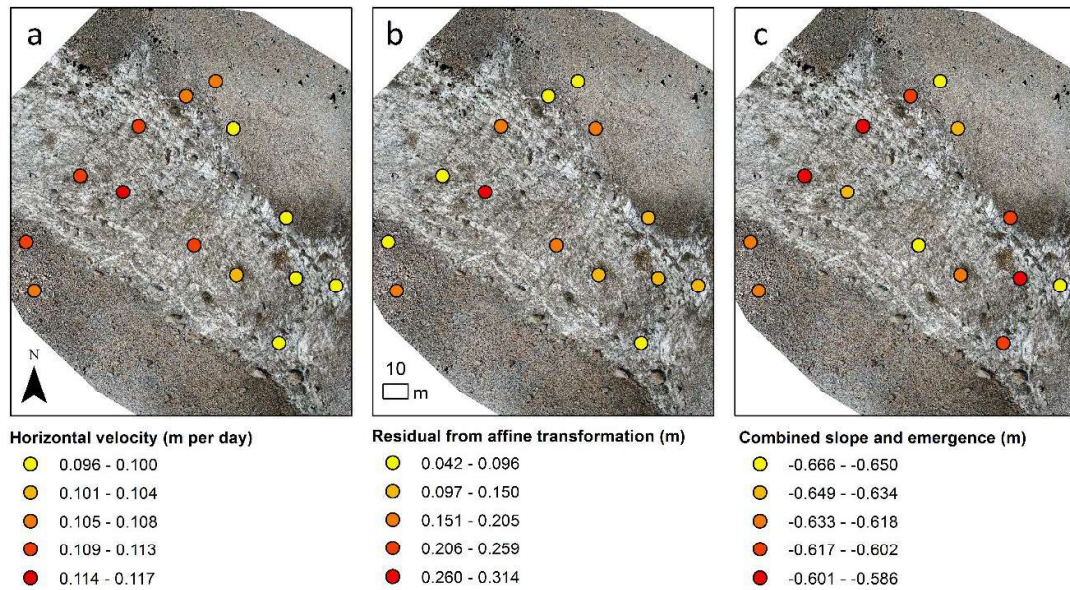


Figure S1 a) Spatial variation in horizontal velocity at each of the stakes used to apply the horizontal transformation of the August DEM to overly the July DEM, b) the residual error for each stake location after the application of the first order (affine) transformation, and c) the combined slope and emergence value derived for each stake.

Table S1 Mean residual errors of UAS-SfM derived products, in metres. Please see text sections 2.2.2 and 2.3.1 for details of how these errors were derived.

	JULY 2017	AUGUST 2017
<b>X</b>	0.031	0.003
<b>Y</b>	-0.036	0.007
<b>Z</b>	-0.065	-0.038
<b>B (XY)</b>	0.048	0.007

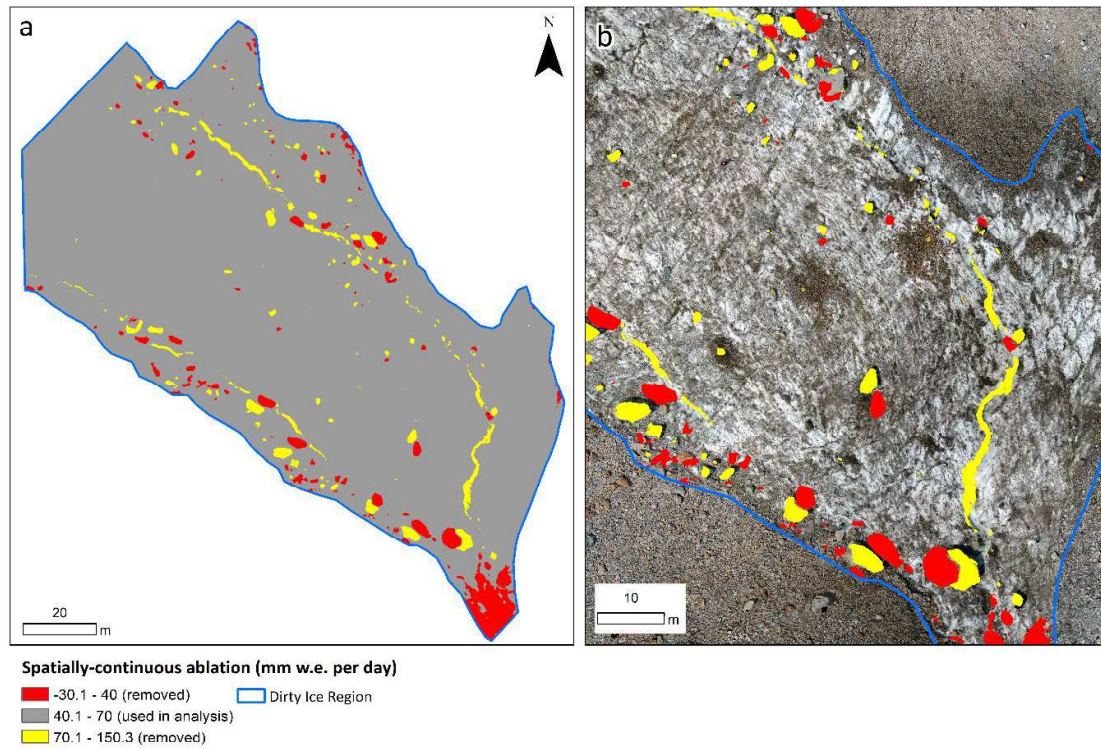


Figure S2 Ablation data removed to reduce errors due to the movement of large boulders. The yellow areas show the boulder positions in July and the red areas show where they moved to in August.

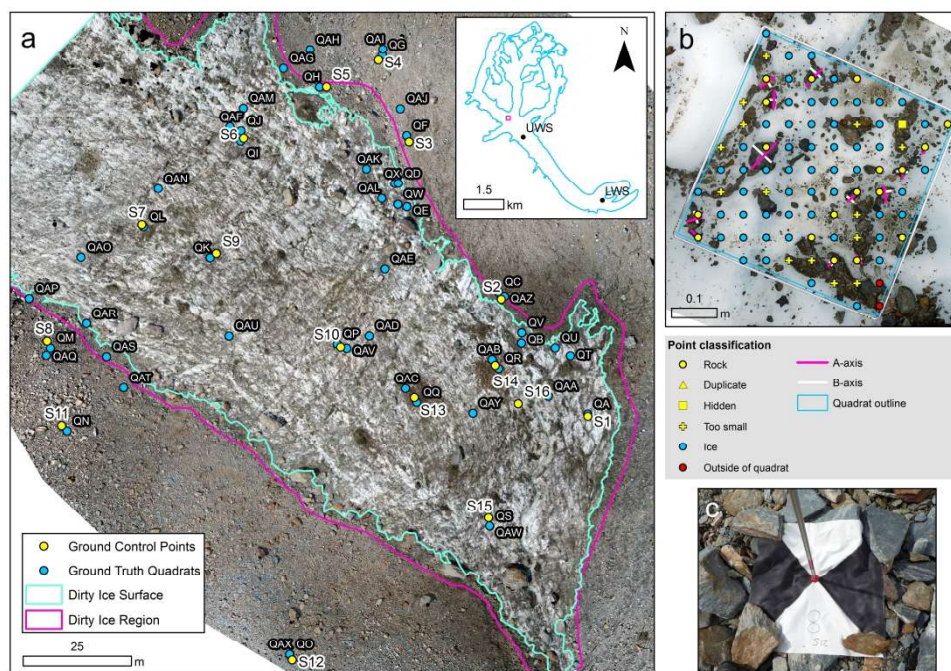
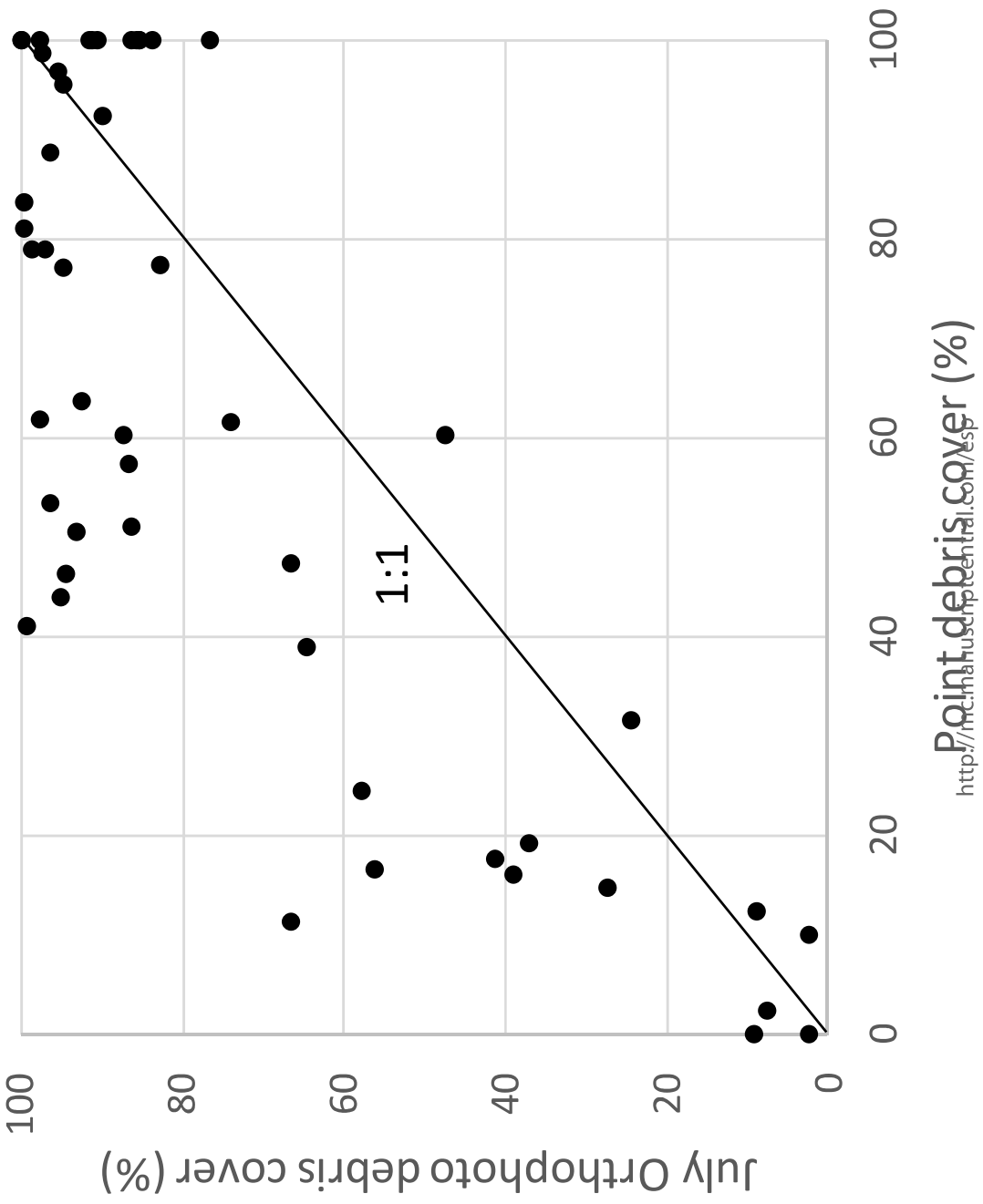


Figure 1 a) Study site map of the dirty ice area showing the location of the ground control points (which were also ablation stakes) and ground truth quadrats, with the inset showing the location of the study site on Miage Glacier and the location of the upper and lower weather stations (UWS and LWS, respectively). Quadrats named 'Q\*' were photographed on 19/07/2017 and quadrats named 'QA\*' were photographed on 22/07/2019, with their albedo also measured. b) Example of the classification of the sample points on the ground truth photographs. The example shown is of quadrat QA. All the yellow points would be classified as debris to determine the percentage debris cover using the point method. c) Photograph of a control point flag over a stake. The red cap is resting on the top of the stake and the total station survey pole is located in the centre of the cap.

Earth Surface Processes and Landforms



<http://mc.manuscriptcentral.com/esp>

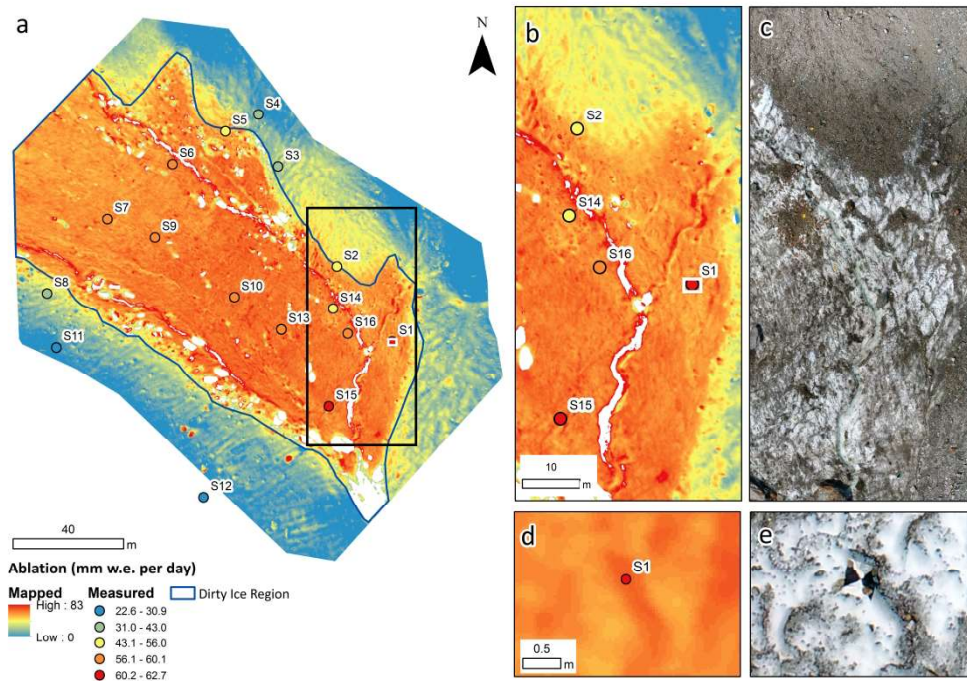


Figure 3 Spatially-continuous ablation over the study area between the 17th of July and 22nd of August. Insets b and d show subsets indicated by rectangles on the ablation map, with insets c and e showing the July orthophoto for the same area. Note that within the dirty ice region ablation <40 mm w.e. per day or >70 mm w.e. per day has been removed to reduce the influence of boulder movement on the ablation data used for analysis. This has also affected some cells of very high ablation following the main supraglacial streams. Negative values outside the dirty ice area were also removed.



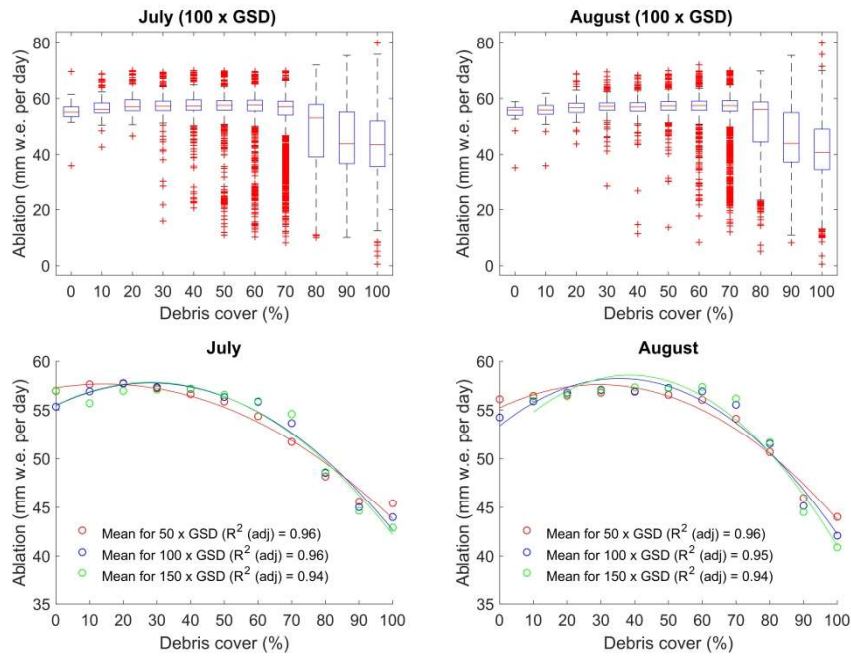


Figure 5 Relationship between orthophoto percentage debris cover and ablation. Subplots a) and b) show boxplots of ablation, split by the orthophoto debris cover rounded to the nearest 10%, (for July and August, respectively) at a 100 x GSD scale. In subplots c) and d) the mean ablation for each 10% group of orthophoto debris cover (for July and August, respectively) is shown at a range of scales (50 x, 100 x and 150 x GSD). Quadratic relationships are shown as they have higher  $R^2$  values than their straight-line equivalents, with  $p < 0.001$  in all cases. The data cover the entire study area, except within the dirty ice region where ablation less than 40 mm w.e. per day or greater than 70 mm w.e. per day was removed to reduce the influence of boulder movement on analysis.

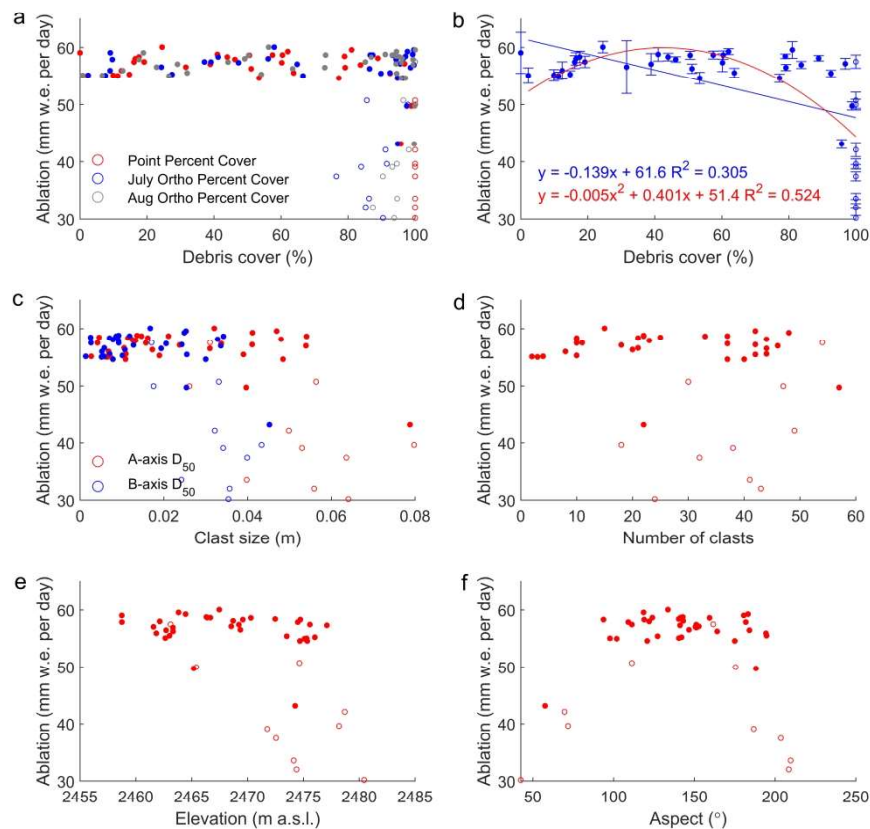


Figure 6 Quadrat ablation against a) percentage debris cover derived using different methods, b) point percentage debris cover, c) clast size, d) number of clasts measured, e) elevation and f) aspect. Closed circles are for quadrats with a partial percentage debris cover (<100% using the point percentage cover) and open circles are those with a complete cover. The variation in percentage cover of low ablation points in panel a) will be due to the misclassification of light-coloured debris as ice. In panel b) error bars show the maximum and minimum ablation within the quadrat and the linear (blue) and quadratic (red) relationships, both significant with  $p < 0.05$ . These relationships do not include QS (0% debris cover) since its ablation was partly altered by a stream, resulting in the wide ablation range for this point.

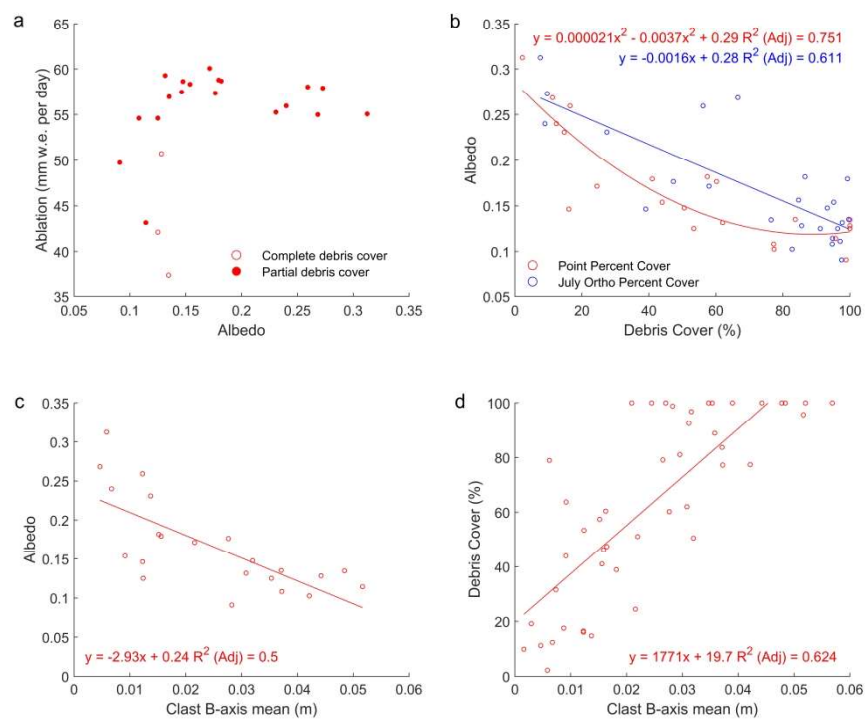


Figure 7 Quadrat albedo against a) quadrat ablation, b) percentage debris cover and c) clast size. Plot d) shows the relationship between point percentage debris cover and clast size ( $r_s = 0.798$   $p < 0.01$ ,  $R^2$  (adj) = 0.624  $p < 0.01$ ). Where linear or quadratic regressions are shown the relationships are significant with  $p < 0.01$  in all cases.

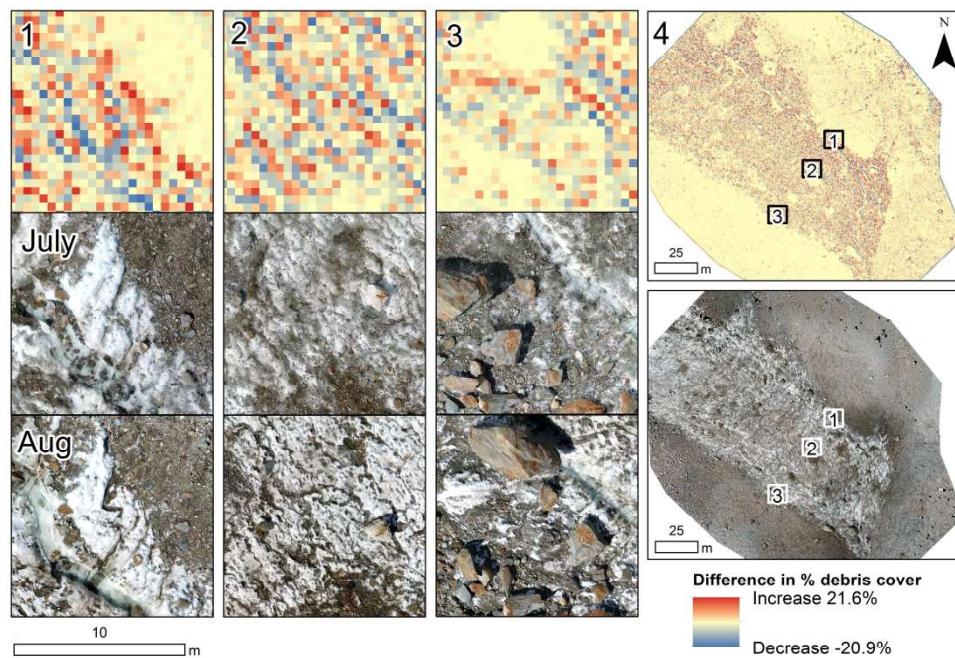


Figure 9 Small scale debris cover change. Each column 1 to 3 covers the same area, as marked in panel 4. The top row shows the change in percentage debris cover at 50 x GSD (where a positive debris cover difference marks an increase in percentage debris cover), the second row shows the orthophoto in July and the bottom row shows the orthophoto in August. The August orthophoto used to determine percentage debris cover was corrected for the horizontal movement of the ice.

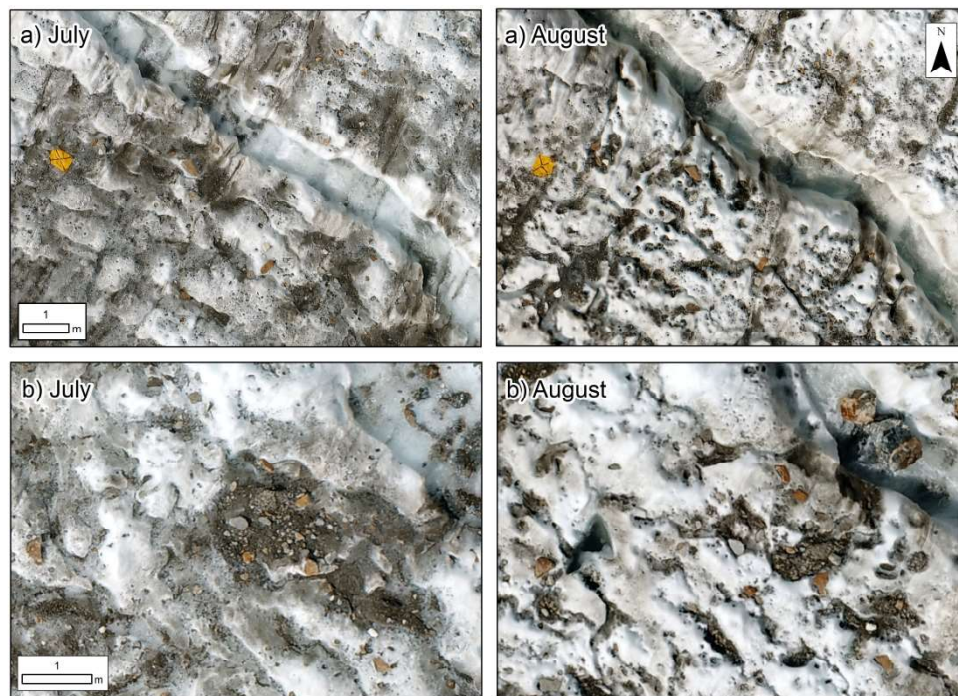
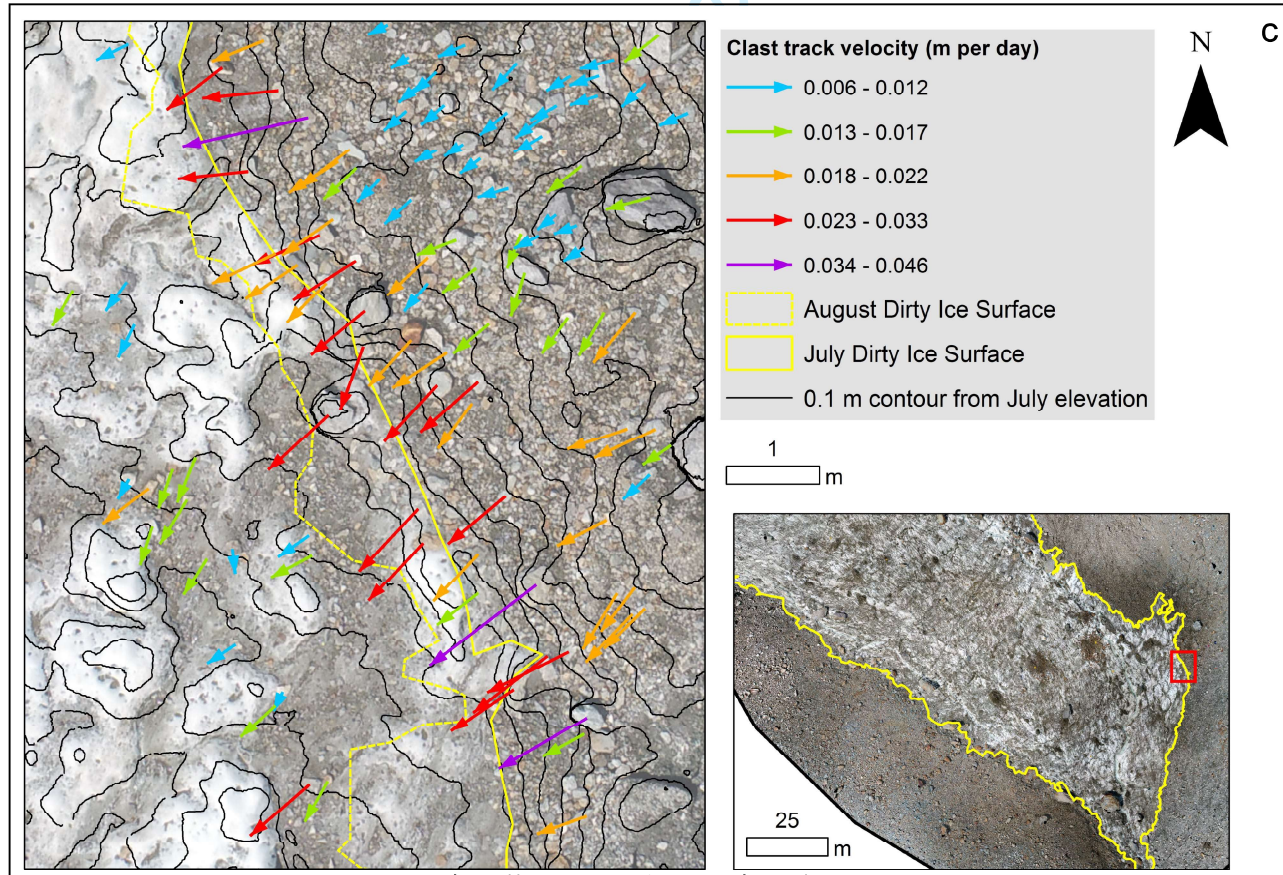
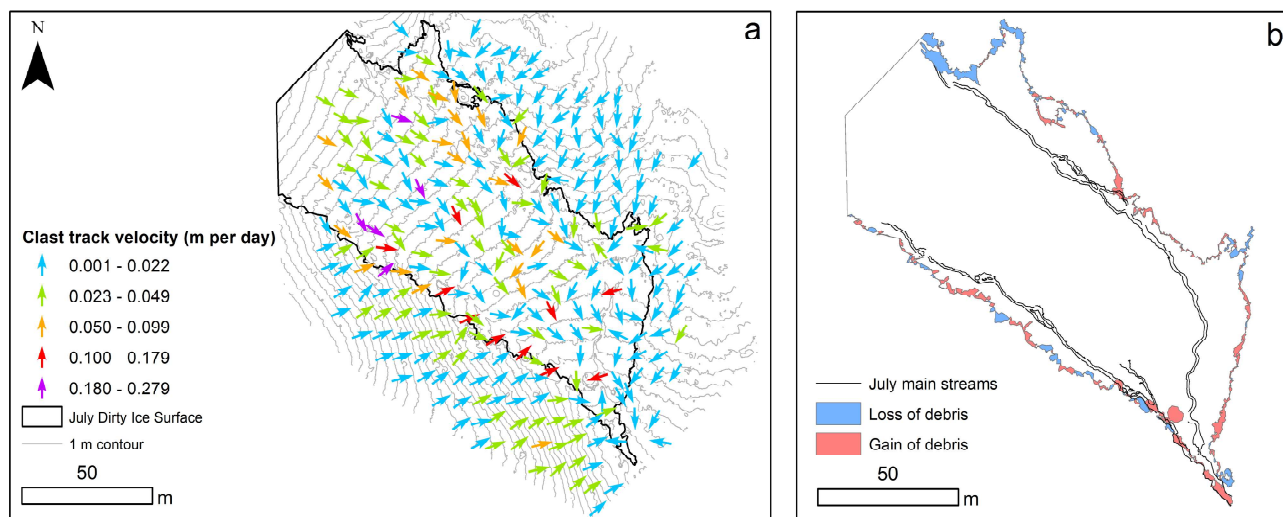


Figure 10 Ice surface evolution, a) showing the redistribution of debris from crevasse traces and b) the concentration of clasts into hollows and streams alongside the removal of fine debris from ice. July and August frames show the same area of the ice surface.

1650x1166mm (72 x 72 DPI)



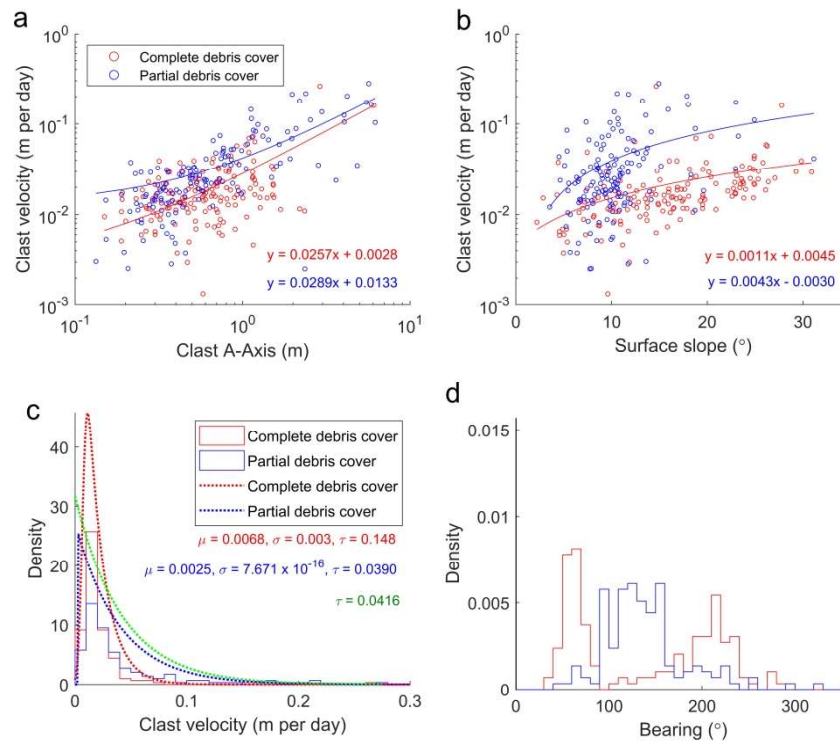
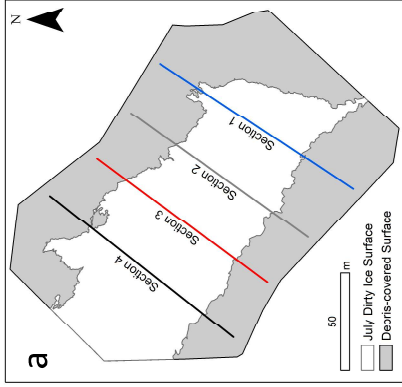
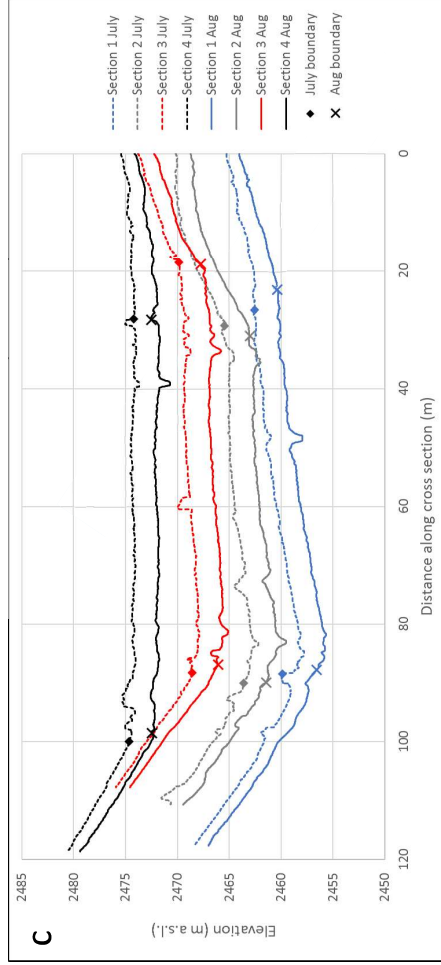


Figure 12 Clast feature tracking, with a) relationship between clast velocity and clast A-axis length (note logarithmic x and y-axis), b) relationship between clast velocity and slope (note logarithmic y-axis), c) histogram of clast velocities with exponentially modified Gaussian distributions overlaid (fitted using Matlab code by Zandbelt (2014)), although the clast velocities can also be modelled with an exponential function (in green) for the partial debris cover, and d) histogram of bearings of clast movement vectors. All relationships shown are significant with  $p < 0.001$ .

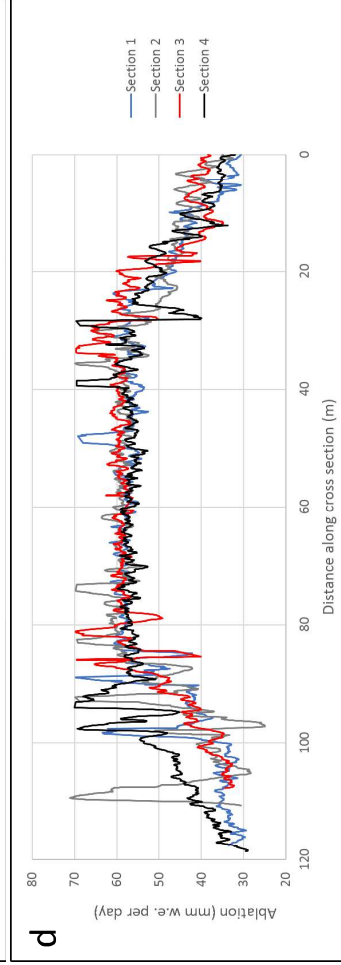


Slope	$D_{top}$ (m)	$D_{bot}$ (m)	$m_j$ (°)	$m_a$ (°)	$\Delta m$
Section 1 East	0	21	7.39	9.42	2.03
Section 2 East	12	25	14.02	14.56	0.54
Section 3 East	0	16	10.88	11.92	1.05
Section 4 East	0	24	2.95	5.17	2.22
Section 1 West	118	92	19.80	20.48	0.68
Section 2 West	111	91	19.53	20.65	1.12
Section 3 West	108	90	21.49	23.13	1.64
Section 4 West	119	101	17.99	20.44	2.45

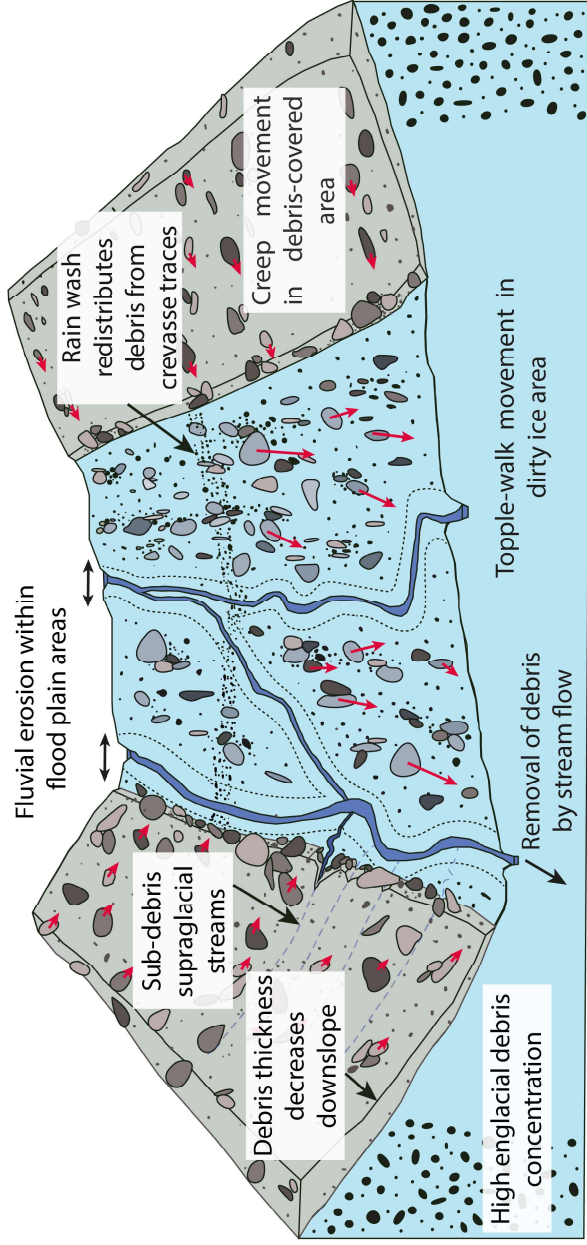
**b**



**c**



**d**



### Debris supply

- Primary supply from melt out of englacial crevasse traces.
- Secondary dispersal from moraine slopes onto dirty ice area.

### Debris transport

- Clasts washed by rain or melt water into hollows and streams. Floods may remove larger clasts and prevent debris encroachment into the dirty ice area.
- Clast creep down debris-covered moraine slopes.
- Topple-walk clast movement on the boundary of and within the dirty ice area.

### Debris removal

- Supraglacial streams transport clasts into the hydrological system, and eventually out of the glacier. Re-entrainment into the ice possible.